Pacific Northwest
NATIONAL LABORATORY

PNNL-34986

Preliminary HEA Solid Phase Processing Development Report

September 2023

Isabella van Rooyen
Ayoub Soulami
Lei Li
Mohan Nartu
Subhashish Meher
Jonathan Wierschke
Jorge Dos Santos
Mageshwari Komarasamy

M4FT-23PN060101061

U.S. DEPARTMENT OF ENERGY

Prepared for the U.S. Department of Energy
under Contract DE-AC05-76RL01830

DISCLAIMER

PACIFIC NORTHWEST NATIONAL LABORATORY
operated by
BATTELLE
for the
UNITED STATES DEPARTMENT OF ENERGY
under Contract DE-AC05-76RL01830

Printed in the United States of America

Available to DOE and DOE contractors from
the Office of Scientific and Technical Information,
P.O. Box 62, Oak Ridge, TN 37831-0062
www.osti.gov
ph: (865) 576-8401
fox: (865) 576-5728
email: reports@osti.gov

Available to the public from the National Technical Information Service
5301 Shawnee Rd., Alexandria, VA 22312
ph: (800) 553-NTIS (6847)
or (703) 605-6000
email: info@ntis.gov
Online ordering: http://www.ntis.gov

PNNL-34986

Preliminary HEA Solid Phase Processing Development Report

September 2023

Isabella van Rooyen
Ayoub Soulami
Lei Li
Mohan Nartu
Subhashish Meher
Jonathan Wierschke
Jorge Dos Santos
Mageshwari Komarasamy

Prepared for
the U.S. Department of Energy
under Contract DE-AC05-76RL01830

Pacific Northwest National Laboratory
Richland, Washington 99354

Summary

The development of high temperature fuel cladding materials to withstand a variety of extreme environments have received much attention. Several potential materials systems that have been identified for the fuel systems and core structural materials application in advanced reactor systems are ferritic/martensitic steel (e.g., HT9), austenitic stainless steels (e.g., 316 LN), oxide-dispersion strengthened steels (e.g., 12 YWT), Ni-based alloys and ceramic-based composites depending on the type of the reactors. Though these material systems have promising properties conducive for radiation-resistant performance, they suffer beyond the design-limit from one or more damage processes such as void swelling, radiation embrittlement, phase instability, corrosion, and limited creep life. A critical necessity exists to design materials systems with better performance than the conventional materials for the advanced reactor systems. Additionally, the drive is further through enabling advanced manufacturing techniques, to decrease the energy used for manufacturing of these components.

In this work, a direct customizable thin-walled tubular product will be developed from irradiation-tolerant composite high-entropy alloys (C-HEAs) with enhanced high-temperature strength and compatibility in a variety of corrosive environments. We will use solid phase processing (SPP) methods to enable development of a robust tube manufacturing process with upscale potential for a U.S.-based tube supply chain. Tube fabrication processes for HEA alloys are still in early research and development phases because it is difficult to prevent segregation on the bulk scale. Furthermore, the presence of nanocomposites can further complicate the manufacturing processes because homogenous distribution of the nano features must be confirmed, and feature coarsening must be prevented during the manufacturing processes.

ShAPE is a complicated thermomechanical process that involves large material deformation, complex die/billet contact, and copious heat generation to maintain the processing temperature. Process modeling of ShAPE can help understand the associated physics, reveal the process parameter/condition relationship, and design for optimized tooling geometries and process parameters. Based on the preliminary process modeling results, it was shown that the Smoothed Particle Hydrodynamics (SPH) model can predict material flow and morphology, stress-strain state, temperature, extrusion force, and torque of the ShAPE extrusion of HEA tubes with various die designs and process parameters. Using the developed SPH model, the thermomechanical physics associated with the ShAPE extrusion of HEA tubes can be better understood. For example, the steady-state process conditions (e.g., force, torque, multi-point temperature) of the ShAPE extrusion of HEA tubes measured from the experiment (planned for the next couple of months) can be used to further improve the SPH model in terms of cooling boundary conditions, stick-slip contact conditions, and thorough model validations.

To date, raw material billets were received, homogenization heat treatment were performed, and microstructural analysis was completed. As part of the corrosion mitigation design strategy, an invention was developed under a provisional patent, to form radially gradient material that can be used as an input material for the tube manufacturing ShAPE process.

Acknowledgments

The research presented here was supported by the Advanced Materials and Manufacturing Technology (AMMT) program of the DOE Office of Nuclear Energy. PNNL is a multi-program national laboratory operated for the U.S. Department of Energy (DOE) by Battelle Memorial Institute under Contract No. DE-AC05-76RL01830.

Acronyms and Abbreviations

AM	additive manufacturing
APR	advancing speed per revolution
DIC	differential interference contrast
FGM	functionally graded materials
FSAM	friction stir additive manufacturing
HEA	high-entropy alloy
HIP	hot isostatic pressing
JC	Johnson-Cook
ODS	oxide-dispersion strengthened
PM	powder metallurgy
PNNL	Pacific Northwest National Laboratory
SEM	scanning electron microscope
ShAPE	shear assisted processing and extrusion
SPH	smoothed particle hydrodynamics
SPP	solid phase processing
SPS	spark plasma sintering
XRD	X-ray diffraction

Contents

Figures

Tables

1.0 Introduction

In this work, we will develop a direct customizable thin-walled tubular product from irradiation-tolerant composite high-entropy alloys (C-HEAs) with enhanced high-temperature strength and compatibility in a variety of corrosive environments. We will use solid phase processing (SPP) methods to enable development of a robust tube manufacturing process with upscale potential for a U.S.-based tube supply chain.

1.1 Scope

Focus of the work will be on the tube manufacturing process and property enhancement enabled by two low-energy SPP processes for a recently developed irradiation-resistant alloy, $NiCoFeCrCu_{0.12}$ [1]. This alloy contains a high density of Cu-rich nanoprecipitates distributed in the HEA matrix, showing excellent void swelling resistance and negligible radiation-induced hardening upon irradiation up to high radiation doses (i.e., higher than 100 dpa), which is significantly better than NiCoFeCr concentrated solid-solution alloys and austenitic stainless steels.

Tube fabrication processes for HEA alloys are still in early research and development phases because it is difficult to prevent segregation on the bulk scale. Furthermore, the presence of nanocomposites can further complicate the manufacturing processes because homogenous distribution of the nano features must be confirmed, and feature coarsening must be prevented during the manufacturing processes.

HEA tube manufacturing processes have not yet been investigated and developed through a combination of SPP processes. To address this need, the proposed work will develop a first-of-its-kind multiple integrated deformation-based manufacturing process that could provide an economic pathway and the flexibility needed for adopting high-irradiation cladding applications.

The two low-energy-intensity SPP manufacturing approaches toward microstructure homogenization that will be deployed are shown in Figure 1. Shear assisted processing and extrusion (ShAPE™) is an SPP technique that adds an additional shear force compared to conventional extrusion approaches (Figure 2). Significant advantages of ShAPE™ are that it can be free from feedstock pre-consolidation and preheating, it is more energy-efficient, and it produces products with better strength, ductility, toughness, fatigue life, and surface finish [2]. In this proposed research, we will develop another more flexible feedstock manufacturing route that has important benefits for both cost and product performance. These flexible raw materials may include other additive manufacturing (AM) and SPP processes like friction stir AM (FSAM) (other routes for this invention may be explored under continued funding and can be discussed on request as invention disclosures are protected).

Coupled with tube functional design optimization, SPP will be used to increase corrosion resistance through co-extruded multilayered bonded tubing. Alternatively, SPP, can provide both an axial and radial gradient functional tube. SPP tube forming allows for continuous transition to a more economic material, reducing welded sections and simplifying welding of tubing to other components. The proposed work will co-extrude Cr with nanocomposite HEAs to provide corrosion protection—based on the application, the Cr cladding can be applied either along the inside or outside of these tubes using the ShAPE process.

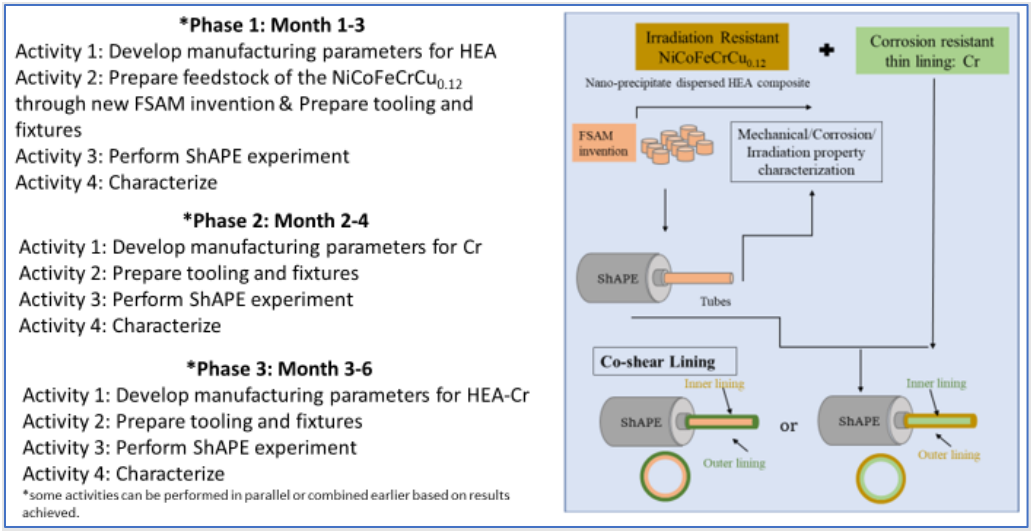

Figure 1. The scope of the proposed work consists of the following two main approaches that will be performed in three phases: (1) direct tube manufacturing of the irradiation-resistant HEA composite with increased strength, (2) co-shear lining manufacturing process for the increased strength and corrosion-resistant, irradiation-tolerant HEAs.

(a) 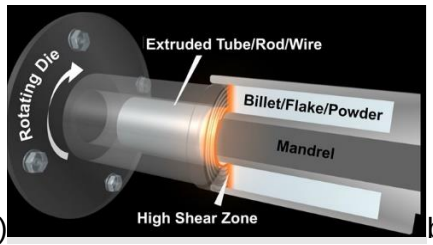

b) 

Figure 2. (a) The ShAPE process uses shear to locally heat, consolidate, and extrude materials. (b) The world's first dedicated ShAPE machine at Pacific Northwest National Laboratory (PNNL).

1.2 Background and Current State-of-the-Art Technologies

Depending on alloy systems and compositions, precipitation of secondary intermetallic compound within the HEA matrix may be possible, further enhancing the mechanical strength and irradiation resistance. Keeping the strengthening ceramics and intermetallic phases at nanoscale will maximize the interfacial area density and toughen the composite. These AM techniques need to capitalize on the benefits to produce C-HEMs with controlled grain sizes and desired reinforcement distributions for enhanced creep resistance, irradiation resistance, and chemical stability of conventionally manufactured alloys. This potential for property enhancement exists for AM processing techniques that can develop materials with tailored microstructures ideal for enhanced physical and/or mechanical properties.

Advantages for using SPP Manufacturing for this development. (1) ShAPE™ has been demonstrated for a variety of materials, including aluminum, magnesium, copper, metal matrix composites, steel, and oxide-dispersion strengthened (ODS) steel. Research shows improved mechanical properties, fewer processing steps, and lower energy intensity through reduction or elimination of additional thermal processing [3]. (2) Co-extrusion was successfully demonstrated

[4] via the ShAPE process on various alloys systems including co-extrusion of 7075 Al with 1100 Al, pure Cu with pure Ni, and Ni with Zircaloy-4. (3) Tooling and fixtures required for ShAPE of 316H stainless steel (SS) have been developed. (4) Ni-based alloys are widely used for high-temperature applications on account of their superior creep strength and oxidation resistance, although this poses a limitation for high neutron flux applications due to its neutron cross section. FeCrAl-based alloys are used but do not provide high-temperature strength in reactor applications either.

Corrosion Behavior. Some research has been performed to study the corrosion characteristics of HEAs. One of the difficulties in fully characterizing their corrosion behavior is the wide variety of stoichiometries in the HEAs and the variety of corrosion environments. Thus, even though the literature exists, it may be difficult to determine how closely it applies to other materials and environments of interest. Overall, the literature seems to indicate that the corrosion behavior of HEAs is superior to many carbon steels and aluminum alloys.

For this work, we are interested in the $NiCoFeCrCu_{0.12}$ HEA studied by Kombaiah et al. [1] Although there may limited work performed on this alloy, we can still look at the effect of the different alloying elements on the corrosion behavior of other HEAs. Following are key points for the design and manufacturing approach to minimize corrosion: (1) Chromium is a key element in the corrosion resistance of stainless steels. As chromium concentration increases, the steels start to form a Cr oxide/hydroxide passivation layer on the surface. It is anticipated that Cr will display similar passivation effects in HEAs [5]. (2) Nickel can be added to stainless steels to stabilize the austenite phase and improve corrosion resistance. However, there appears to be a limit to the amount of Ni that is beneficial to corrosion resistance. Beyond this limit, corrosion rates have been reported to increase. (3) Copper is primarily added to steels to improve mechanical properties despite its negative impact on corrosion resistance. The effect on corrosion is affected by the microstructure of the copper-containing phases. Copper-containing alloys form interdendritic phases that are preferentially dissolved. (4) A study of corrosion in $FeCoNiCrCu_x$ HEAs (with x = 0, 0.5, and 1) showed that corrosion preferentially occurred at these interdendritic phases [6]. (5) Processing methods, including aging treatments, have also been carefully selected to achieve selected mechanical and even corrosion-resistant properties. The manufacturing of extruded HEAs using ShAPE will plausibly influence the corrosion behavior of these materials.

1.3 Tasks

Tasks are based on the project scope as indicated in Figure 1. As mentioned in the description of the various phases in Figure 1, some work can be done in parallel or even simultaneously. Therefore, this section describes the main tasks.

1.3.1 Develop Process Parameters for Phases 1–3

The current knowledge provides a strong foundation for our work—however, it can be noted from Figure 3 that the materials we are planning to fabricate in tube form fall well outside the envelope of the materials previously manufactured and would provide significantly improved know-how to the community. This will be a high-strength material SPP application with possible new challenges. A previously developed smoothed particle hydrodynamics (SPH) modeling framework [7,8] will use prior tube-forming material parameters to find an initial starting parameter window for new material types. The SPH model accurately predicts material flow, stress-strain, temperature, strain rate, and grain size given certain process parameters for various advanced manufacturing techniques, such as ShAPE™ and friction extrusion of

aluminum alloys, ShAPE™ of multi-alloy cladded tubing with dissimilar materials such as 1100/6061/7075 and Cu/Ni, friction stir welding/processing welding/processing (FSW/FSP) of aluminum alloys and stainless steels, and cold spray of Mg/Zn material systems. Prior experiences of producing bars through high-shear extrusion processes show that the SPP can be applied to materials that elastically deform and are thermally and chemically compatible with the tooling [7].

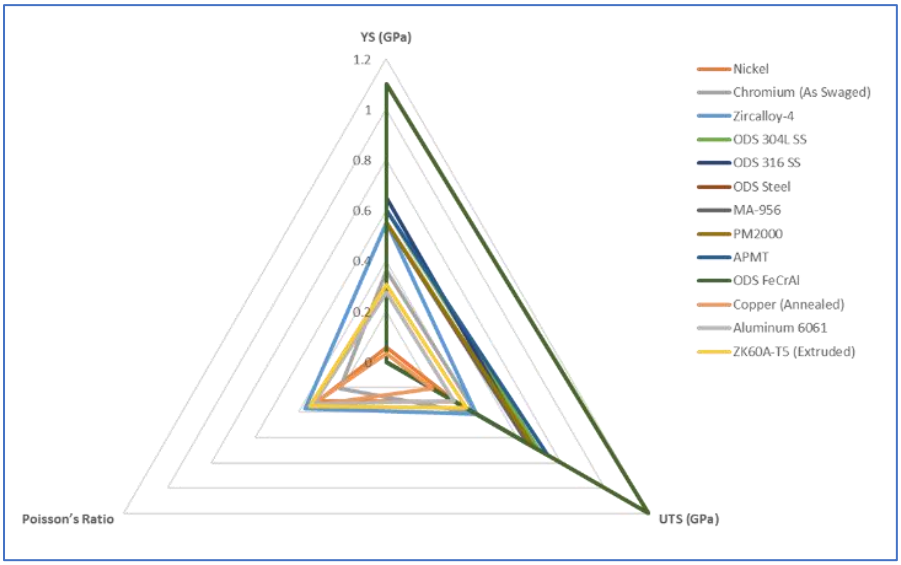

Figure 3. Property envelope of the materials previously considered for cladding or materials that have already been used by PNNL for tube and bar manufacturing via the ShAPE™ process.

1.3.2 Prepare Feedstock of the $NiCoFeCrCu_{0.12}$ through New FSAM Invention & Prepare Tooling and Fixtures

This section contains proprietary information and cannot be described fully at this time.

1.3.3 Perform ShAPE Experiment

Tooling design and optimization is a key part during the execution stage. Although lessons learned from prior work will be utilized, material compatibility studies will be performed. The benefits of ShAPE™ for this project include the following: (1) low fabrication temperatures, eliminated melt-related defects such as porosity and cracking typically associated with casting or AM techniques, decreased segregation of elements, refined grains, and prevented dissolution or growth of precipitates, (2) the homogenous equiaxed grain microstructure, because the thermokinetics of ShAPE remain unchanged throughout fabrication, (3) nanoprecipitates homogenously distributed and/or engineered for alignment and strength, irradiation behavior, and thermal conductivity, (4) design and formation of other non-reactive nanostructures for improved irradiation resistance and strength (not fully demonstrated; may cause clustering during initially)—we should not have problems making iron-based 20–100 nm oxide composites using powder-mixing methods, and (5) enhanced corrosion protection may not be fully achieved by compositional and homogenized microstructures due to competing requirements. Therefore, by implementing co-shear lining tube manufacturing processes and gradient tube processes, prior art on Ni-liners were demonstrated using Zircaloy.

1.3.4 Performance Evaluation and Validation

As a benchmark, Fe-based alumina-forming alloys still do not provide sufficient mechanical strength in corrosive environments for high-temperature applications in advanced nuclear reactor systems. Performance evaluation of tubes produced by ShAPE includes the following.

1. Mechanical properties (e.g., high-temperature nano indentation [due to the short time frame and feasibility objectives of this work, no tube burst/creep or tensile tests will be performed]).
2. Microstructure examination using X-ray diffraction (XRD), scanning electron microscopy, transmission electron microscopy, and atom probe tomography. Because nano distribution and segregation are key factors in irradiation performance, high-resolution evaluations are required, as well as interfacial features.
3. Corrosion tests: The corrosion of materials depends on more than just the chemistry of the material and the environment. The microstructure of the material can have a significant impact on oxidation [9], pitting [10], stress corrosion cracking [11], and diffusivity of species into the bulk material [12], among other electrochemical and mechanical effects. The manufacturing process that the material goes through will influence the final microstructure. The use of friction extrusion in manufacturing is no exception [13]. With the increased interest in the use of friction extrusion, it is important to understand just how this process affects the corrosion potential of the materials.

To better understand the magnitude of the effect that ShAPE manufacturing has on the corrosion behavior of materials, accelerated static corrosion testing can be performed. Samples of alloys manufactured by ShAPE as well as commercially available samples of the same alloy can be placed in small Parr pressure vessels. The use of multiple vessels will allow for corrosion to be tested in different environments and temperatures. After exposure, the samples can be tested using XRD and time-of-flight secondary ion mass spectrometry or LA-LIBS to analyze the structure and thickness of the oxide layer that has formed. For this study, it is recommended that two different materials be tested per environment for at least two separate environments. It is also recommended that one environment be run twice at different temperatures. This will generate 12 samples.

For the FY 2023 work scope and initial feasibility studies, it will not be possible to perform high-temperature ion irradiation tests at 800 °C at various displacement per atoms (dpa) to get an initial trend on localized irradiation performance. It is highly recommended to perform these in follow-up work.

1.4 Expected Results of the FY 2023 Scope

The primary goal of the FY 2023 scope is to show the feasibility of a manufacturing route that will be scalable for HEA cladding with further optimization. Additionally, by applying this specific method (ShAPE™), we would verify if the manufacturing technically applied here, further enhances the mechanical properties of the HEA material.

1.5 Follow-on Funding Opportunities

This proposed work will still be in an early technology readiness level and would need optimization. To fully optimize the process, it is recommended to continue with the high-temperature irradiation, high-temperature creep, and mechanical testing in the following year

after optimized batch tubes were produced. Continued study of the corrosion behavior of these materials, particularly after irradiation and under load, is also recommended.

Additionally, future work can include even further expansion into refractory HEA for extreme high-temperature applications that may include carbide strengthen Nb-rich HEA composites. Additionally, PNNL has multiple novel ideas surrounding a variety of composite features that can be explored once the base process of the raw (stock material) via the new processes has been tested to be feasible.

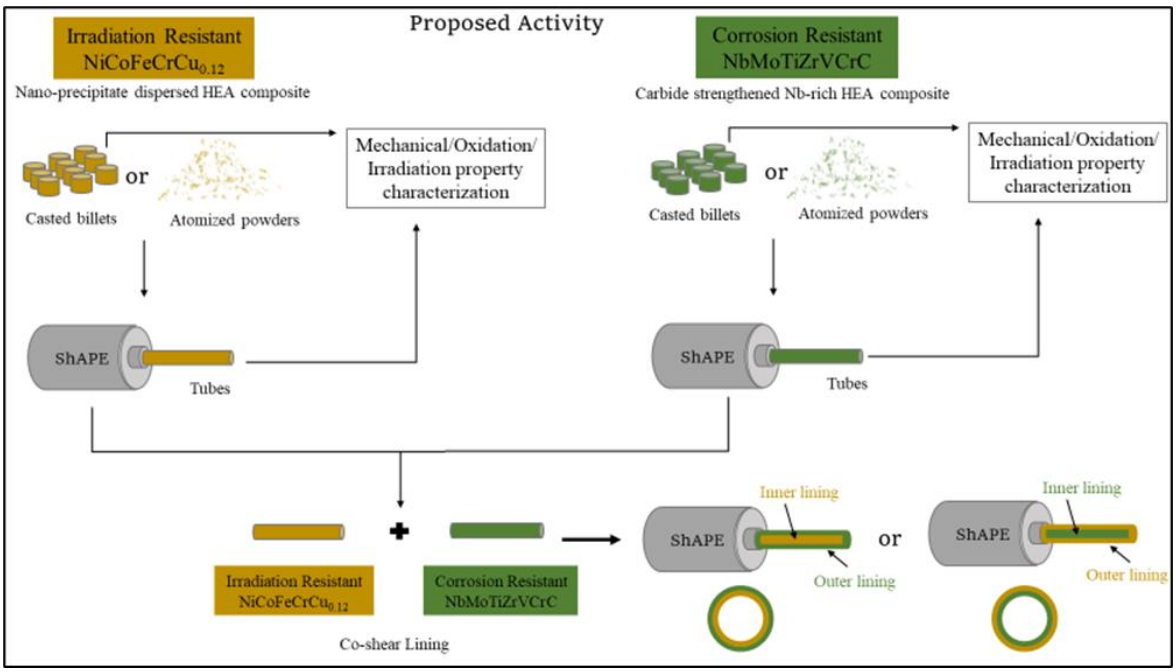

Figure 4. Next-generation experimentation and expansion of the FY 2023 work scope into refractory HEA and future extreme high-temperature applications for tube manufacturing via ShAPE™ at PNNL.

2.0 SPH Modeling to Identify ShAPE Process Parameter Window

ShAPE is a complicated thermomechanical process that involves large material deformation, complex die/billet contact, and copious heat generation to maintain the processing temperature. Process modeling of ShAPE can help understand the associated physics, reveal the process parameter/condition relationship, and design for optimized tooling geometries and process parameters.

2.1 Smoothed Particle Hydrodynamics (SPH) Method

Process modeling of ShAPE is a non-trivial task, and conventional mesh-based methods (e.g., finite element method, finite volume method, etc.) could encounter various numerical issues when simulating the process. For example, the Lagrangian mesh-based methods suffer from mesh distortion issues when dealing with large material deformations. Frequent remeshing is typically needed to address this issue, which is computationally expensive and time-consuming. The Eulerian mesh-based methods require extra data tracking algorithms to recover the physical information at arbitrary spatial locations. Moreover, the die/billet interface is not clearly defined in Eulerian methods, leading to inaccurate contact definition during the simulation. Although combined Lagrangian and Eulerian methods (e.g., Coupled Eulerian Lagrangian, Arbitrary Lagrangian Eulerian) have been proposed to alleviate the abovementioned disadvantages of each type of mesh-based methods, the issues persist when the material deformation is extremely large.

On the contrary, SPH is a truly meshfree method that does not rely on any background grid or mesh. It utilizes kernel function to describe interaction between particles, as shown in Figure 5. As a result, it is suitable for modeling large material deformation without having a mesh distortion issue. Moreover, SPH has a Lagrangian description, which makes it easy to track the field variables in each discretized SPH particle. The particle representation of SPH also enables a natural and clear definition of the die/billet interface to apply contact conditions. These features make SPH ideal for ShAPE process modeling. Therefore, SPH will be mainly used in this project to model the ShAPE process of HEA materials. Details about SPH can be found in [8,14] and are omitted herein.

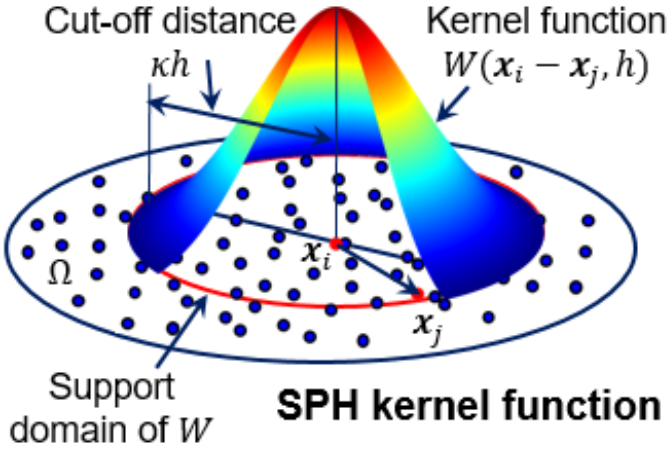

Figure 5. Schematic of SPH kernel function on a 2-D space.

2.2 SPH Model Setup

The SPH model setup for the ShAPE process is described in this subsection. Figure 6(a) shows the schematic of the SPH model setup, which includes an inner container, an outer container, a top die, a bottom die, and a billet ring. The OD, ID, and height of the billet ring are 31.75 mm, 10 mm, and 6 mm, respectively. The diameter of the die extrusion hole is 12 mm, leading to a 1 mm thickness of the extruded tube wall. The containers and dies were assumed to be rigid parts that were discretized into 616,463 solid elements. The billet ring was the only deformable part and was discretized into 2,153,280 SPH particles at 0.125 mm in diameter. To better visualize the material flow, different colors were assigned to the billet ring in the radial direction. The billet containers were stationary, while the dies were rotating and plunging into the billet ring.

To enable heat transfer between SPH particles and rigid parts, ghosted SPH particles [7] were placed in each solid element in the inner container and top die. These ghosted SPH particles will move rigidly with their parent elements and shared the same kernel function with their neighboring deformable billet SPH particles. Therefore, the ghosted SPH particles will only conduct heat from the billet SPH particles. The temperature in the ghosted SPH particles will be shared with their parent solid elements, exchanged with the other rigid parts, and finally interact with the thermal boundary. The idea of ghosted SPH particles is illustrated in Figure 6(b).

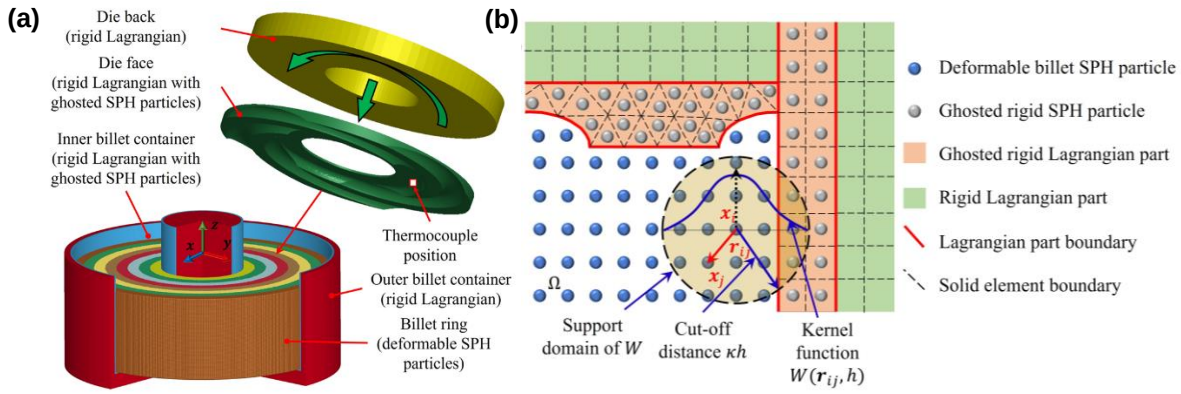

Figure 6. (a) Schematic of SPH model setup for ShAPE, and (b) ghosted SPH setup.

2.3 Material Properties

The HEA billet material was considered as a thermo-viscoplastic solid, and its behavior was described by the Johnson-Cook (JC) constitutive model expressed as

$$\sigma_y = (A + B\varepsilon^n)(1 + C \ln \dot{\varepsilon}) \left[1 - \left(\frac{T - T_r}{T_m - T_r}\right)^m\right] \quad (1)$$

where σ_y is material flow stress, ε is equivalent plastic strain, $\dot{\varepsilon}$ is plastic strain rate, and T, T_m, and T_r are material temperature, melting temperature, and reference temperature, respectively. A, B, and n are model constants describing material strain hardening, C is the strain rate hardening parameter, and m is the thermal softening constant.

JC is a phonological model that needs to be calibrated with material testing data to have good predictivity. Because the stress-strain curves of $NiCoFeCrCu_{0.12}$ HEA materials under various strain, strain rate, and temperature are very rare in the literature, here we considered the $NiCoFeCrAl_{0.3}$ as a surrogate HEA material in the preliminary modeling. Based on the

$NiCoFeCrAl_{0.3}$ material properties shown in [15], the calibrated JC material parameters are tabulated in Table 1. Note that during the calibration process, B and n were fixed to 0 to address the ever-increasing strain-hardening issue in the JC model [16].

Table 1. Calibrated JC parameters for HEA used during process modeling [19].

	A (MPa)	B (MPa)	n	C	m	T_m (°C)	T_r (°C)
$NiCoFeCrAl_{0.3}$	490	0	0	0.015	0.6	1400	24

To accommodate the high-temperature and high-torque conditions during ShAPE of HEA, the Inconel 718 alloy was considered for the billet container material while a W-Re Alloy was used for the die material. The elastic-thermal properties of all materials are listed in Table 2.

Table 2. Elastic-thermal material properties used during process modeling [19,20].

	Density (g/cm^3)	Poisson's ratio	Elastic modulus (GPa)	Heat capacity (J/g-°C)	Thermal conductivity (W/m-°C)
$NiCoFeCrAl_{0.3}$	7.86	0.295	197	0.460	28
Inconel 718	8.17	0.28	140	0.435	26
W-Re	19.55	0.24	403	1.400	70

2.4 Other Model Settings

The contact condition between the die and billet was assumed as partial sticking-slipping, which was modeled by the Coulomb-Tresca friction law, as shown in Figure 7. The friction coefficient was set as 0.6. Heat was generated from 90% of the material plastic deformation and 100% of the die-billet friction sliding energy. A thermal boundary condition was applied on the outer surface of the outer billet container to mimic water cooling during the experiment, with the thermal dissipation coefficient 1 kW/m^2-°C. To reduce the computational time, an initial temperature gradient was prescribed for the SPH model. The billet ring was sectioned into four even slices longitudinally, which were assigned initial temperatures of 480–600 °C with a −40 °C gradient from the billet-die interface to the billet bottom. The initial temperature of dies and containers was set as 600 °C and 400 °C, respectively. Simulations were run on a PNNL research computing supercomputer with appropriate time and mass scaling to further increase the computational efficiency.

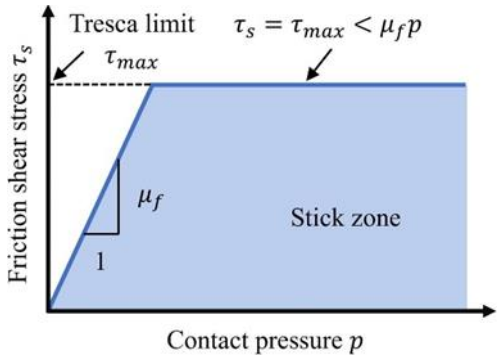

Figure 7. Coulomb-Tresca friction law.

2.5 Parametric Study on Die Geometrical Design

The SPH model was first used to elucidate the effect of die geometries on the material flows and process conditions. To this end, two four-scroll die designs were investigated that have the same geometry, except one with counterbore and another without counterbore. Detailed geometries of these two die designs are given in Figure 8. The processing parameters were set at a 25 mm/min die plunging speed and 50 rpm die rotational speed for this parametric study.

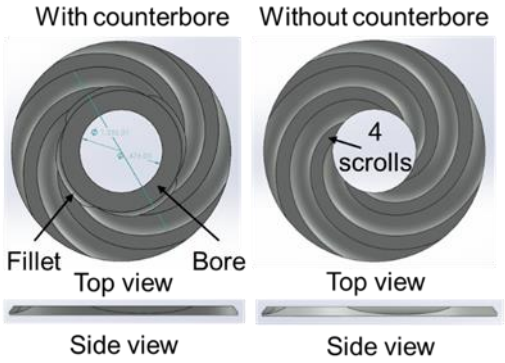

Figure 8. Die designs for parametric study.

The material flow results with different die designs are shown in Figure 9. One can see that both die designs can extrude tubes from the billet ring. As shown in Figure 9(a), the die with counterbore resulted in a tube with an inner wall material mainly from the billet ring inner radius (in red). This is because less material stirring and mixing can be achieved by the die counterbore plateau. The outer wall materials (in brown, yellow, and green) also experienced less stirring and were more evenly cladded on the tube core. On the contrary, a clear material helical pattern can be seen in the die without counterbore in Figure 8. Moreover, the tube wall materials were better stirred and mixed by the sharp corners of the scrolls near the extrusion hole, as shown in the right panel of Figure 9.

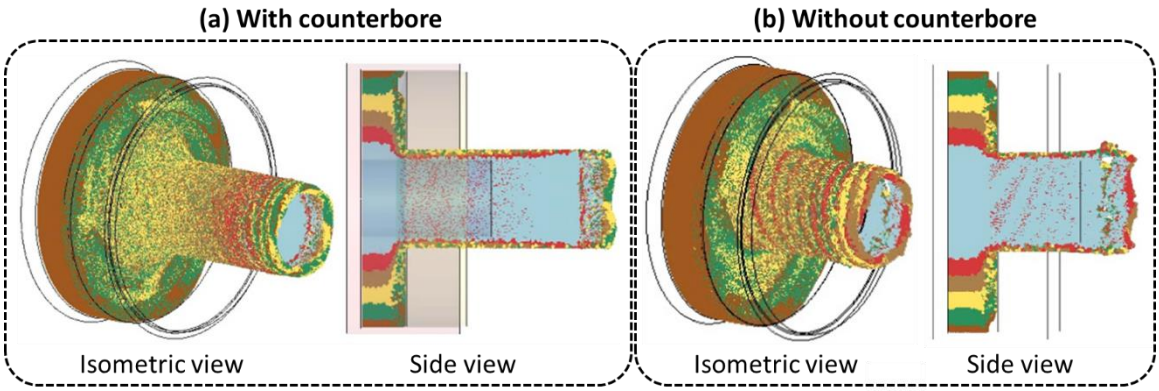

Figure 9. Predicted material morphologies for a die (a) with and (b) without counterbore.

Figure 10 shows the corresponding central cross-sectional temperature and equivalent (effective) plastic strain distributions for the cases in Figure 9. In terms of temperature, both cases exhibited similar temperature magnitudes and distributions in the billet ring. A slightly higher temperature was achieved by the die without counterbore, as shown in Figure 10(b). This is because severe material stirring and mixing occurred in the vicinity of this location where the sharp corners of the scrolls were. As a result, more material plastic deformation took place and released more heat energy to elevate the local temperature therein. This can also be demonstrated by the effective plastic strain plots, where similar plastic strain distributions are seen for both die designs. More plastic deformation occurred in the vicinity of the die extrusion hole and in the tube wall for the die without counterbore, as displayed in Figure 10(b). Because of the sharp corners in the die without counterbore, helical plastic strain distribution was achieved in Figure 10(b), while more uniform plastic strain distribution is observed in the die with counterbore, as shown in Figure 10(a).

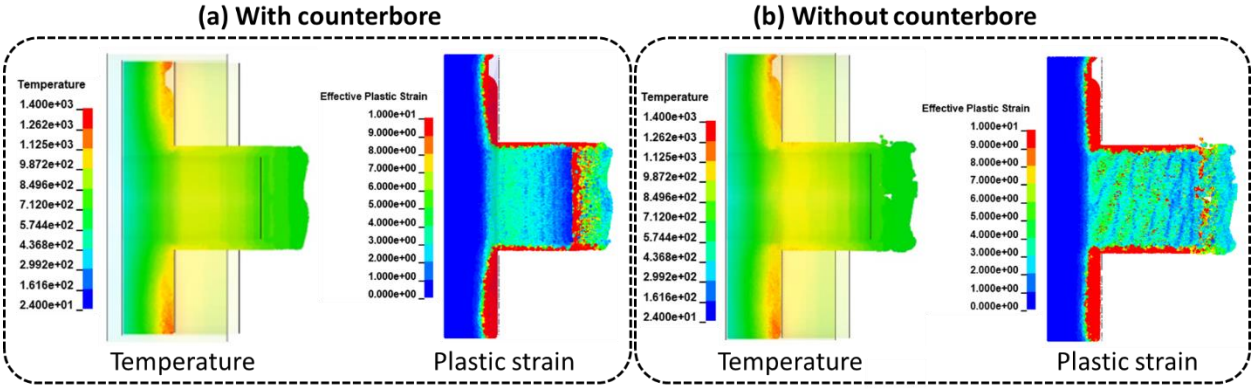

Figure 10. Predicted central cross-sectional distributions of temperature (unit: °C) and effective plastic strains for dies (a) with and (b) without counterbore.

The model-predicted die temperature (location marked as “thermocouple location” in Figure 6(a)), extrusion force, and torque for both die designs are given in Figure 11. The steady state die temperature is similar for both cases, which has already been revealed in Figure 10. The 1100 °C value is within the reasonable range of 900–1200 °C for the ShAPE machine to operate properly. Due to the similar temperature and material flow stress, the extrusion forces are similar for both cases and around 250 kN, as shown in Figure 11(b). The torque value for the die with counterbore is around 325 N·m, while for the die without counterbore, it is about

395 N·m. The difference in torque is primarily because the die without counterbore has a larger circumferential surface area that is in contact with the billet. Thus, additional torque from these extra contact surfaces leads to a larger torque value for the die without counterbore.

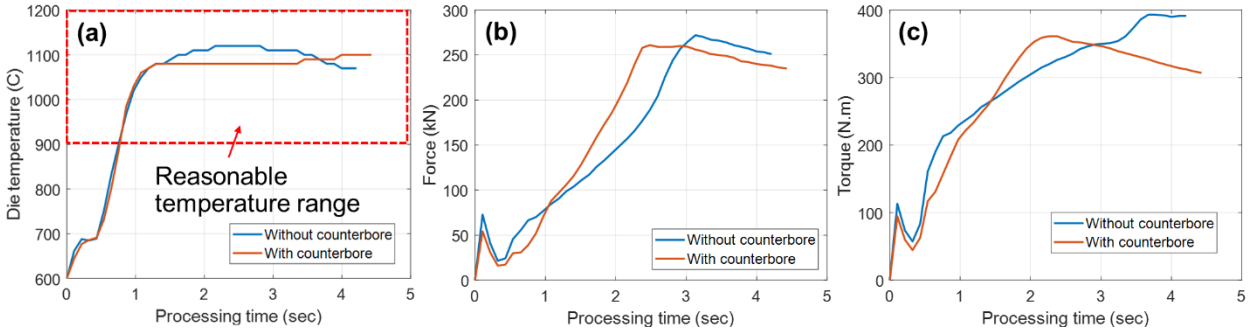

Figure 11. Model-predicted (a) die temperature, (b) extrusion force, and (c) torque histories for dies with and without counterbore.

2.6 Parametric Study on Die Process Parameter Window

After the parametric study on die geometry in Section 2.5, a parametric study on die process parameters was carried out in this subsection. To this end, the die without counterbore was used, and a total of five cases were simulated with different die plunging (advancing) and rotational speeds, as detailed in Table 3. Note that these five cases were selected to have different APR, which means die advancing speed per revolution.

First, the model-predicted material morphologies of a small, extruded tube section in extrusion direction for all cases are compared in Figure 12 with measured material helical angles. When APR is low, such as 0.5 for case 1, a clear helical material pattern can be seen with a 74.1° angle to the extrusion direction. With lower APR, such as 0.25 for cases 2 and 4, the helical angles increased to 82.1° and 79.6°, respectively. This is as expected because a lower die APR indicates more die revolutions per unit extrusion length. As a result, the material helical pattern is prone to being more vertical. If the APR was further reduced to 0.167 in cases 3 and 5, billet materials are well mixed by the die rotation. In these cases, it is hard to distinguish the helical angles, which are obviously larger than 85 °.

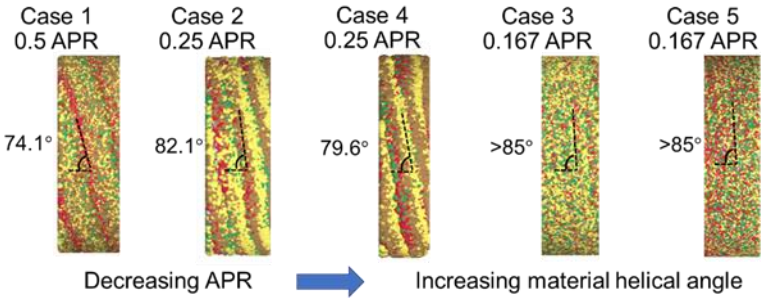

Figure 12. Model-predicted tube wall material helical angles.

Table 3. Summary of modeled cases and predicted processing conditions without die counterbore.

Case No.	Die plunging speed (mm/min)	Die rotational speed (rpm)	Die advancing speed per revolution (mm/rev)	Steady-state die temperature (°C)	Steady-state extrusion force (kN)	Steady-state torque (N·m)
1	25	50	0.5	1102.9	272.1	391.5
2	25	100	0.25	1161.7	167.2	309.4
3	25	150	0.167	1256.3	108.6	272.0
4	12.5	50	0.25	1301.7	130.6	307.3
5	8.33	50	0.167	1351.8	64.9	232.2

Table 3 summarizes the model-predicted steady-state die temperature, extrusion force, and torque for all the cases. The die temperature is the lowest when the extrusion force is highest and the torque in case 1 has the largest APR. This is as expected because larger APR indicates less heat generation and lower temperature. The material flow stress is therefore higher, leading to larger extrusion force and torque. When the die plunging speed is fixed at 25 mm/min, decreasing APR (cases 1, 2, and 3) leads to a higher die temperature, lower extrusion force, and lower torque. The same trend can be seen in cases 1, 4, and 5, when the rotational speed is fixed with decreasing APR. However, with the same APR, a slower die plunging speed results in higher temperature, lower extrusion force, and smaller torque. This is because a lower plunging speed allows enough time for the generated heat to transfer and propagate throughout the billet ring. This can be visually seen in Figure 13—when the die plunging speed is fixed at 25 mm/min, increasing the die rotational speed from 50 rpm (case 1) to 150 rpm (case) increases the overall heat generation and temperature in the billet. With the same APR of 0.167 and rpm of 50, reducing the die plunging speed from 25 mm/min (case 3) to 8.33 mm/min (case 5) significantly increases the temperature in the billet. Based on Table 3, the process parameter window is 25 mm/min at 50–100 rpm to ensure a safe operation temperature ranging from 900 to 1200 °C. Note that this process window can be further refined if there is a special limitation on the machine extrusion force and torque capability.

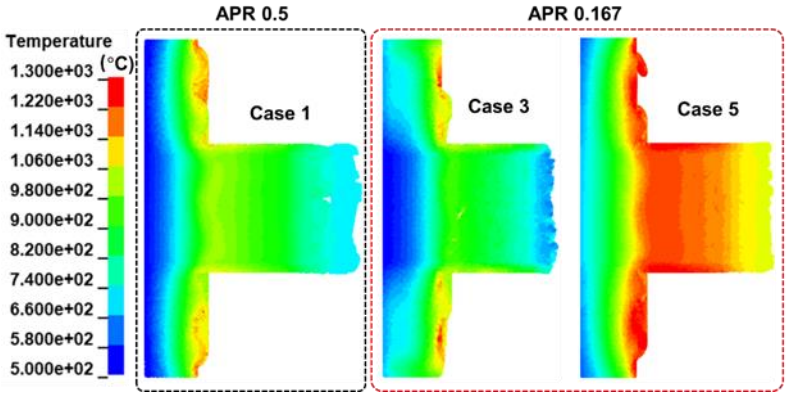

Figure 13. Model-predicted central cross-sectional temperature distribution for cases 1, 3, and 5 without die counterbore.

2.7 Discussion and Outlook

Based on the preliminary process modeling results, it was shown that the SPH model can predict material flow and morphology, stress-strain state, temperature, extrusion force, and torque of the ShAPE extrusion of HEA tubes with various die designs and process parameters. Using the developed SPH model, the thermomechanical physics associated with the ShAPE extrusion of HEA tubes can be better understood. The developed SPH model can also be used to carry out parametric study and design optimization to help identify the appropriate process parameter window and design geometries.

It should be noted that all the preliminary modeling results were still based on the properties of the surrogate HEA material $NiCoFeCrAl_{0.3}$ without experimental validation in terms of process conditions. Future work on the modeling direction includes a uniaxial test or micro-indentation test on the $NiCoFeCrCu_{0.12}$ material sample under different temperatures and strain rates to better calibrate JC model parameters. The thermal properties of $NiCoFeCrCu_{0.12}$, such as heat capacity and thermal conductivity, will also be measured and be incorporated into the SPH model to increase the model predictivity. Moreover, the steady-state process conditions (e.g., force, torque, multi-point temperature) of the ShAPE extrusion of HEA tubes measured from the experiment can be used to further improve the SPH model in terms of cooling boundary conditions, stick-slip contact conditions, and thorough model validations.

3.0 Raw Material Processing Design and Preliminary Results

3.1 Alloy Choice and Phase Diagram

HEAs containing multiple principal elements are known to exhibit good mechanical properties, excellent corrosion, and oxidation resistance and are therefore suitable candidates for various structural applications [17-22]. Recent efforts have been focused on investigating the radiation response of certain HEAs for advanced nuclear energy applications [23]. The NiCrFeMn HEA exhibits a significantly lower void swelling and radiation-induced hardening and segregation at elevated temperatures (400–700 ℃) and 10 dpa compared to conventional FeNiCr-based alloys [24]. When Mn is replaced with Co, the HEA (NiCrFeCo) exhibits 10 times lower radiation-induced void swelling (at 53 dpa) than NiCo-based alloys [25,26]. However, it is argued that the single-phase HEAs, with reasonably simple microstructures like the abovementioned HEAs, reveal significant void swelling and fail to maintain their structural integrity when irradiated at > 50 dpa [26-28]. Considering this, several HEAs with complex microstructures and high-density interfaces were investigated for operation under high radiation doses (> 200 dpa). In a recent study by El-Atwani et al., the formation of Cr- and V-rich secondary precipitates within the BCC matrix resulted in a remarkably lower radiation-induced hardening for the W-based HEA [29].

On the other hand, adding specific elements such as Cu, Al, and Ti can also enhance the radiation resistance of the NiCoCrFe fcc-HEA [30]. The addition of these elements is reported to induce second-phase precipitation in the NiCoCrFe-based HEAs [31-33]. Kombaiah et al. [1] doped the equiatomic NiCoCrFe HEA with three atom % of Cu and fabricated the $NiCoFeCrCu_{0.12}$ HEA using the floating-zone solidification method and subsequentially annealed the HEA to fabricate a microstructure with a high density of interphase boundaries arising from Cu-rich nanoprecipitates. The Cu precipitates act as sink sites for absorbing the point defects generated during irradiation, thereby enhancing the radiation resistance of the $NiCoFeCrCu_{0.12}$ HEA even at higher dosages. For instance, when irradiated with Au ions at 100, 350, and 500 dpa doses at 475 °C, void swelling of only < 0.01% was observed. The resistance to radiation-induced hardening and void swelling of the $NiCoFeCrCu_{0.12}$ HEA is remarkably higher than the NiCoCrFe HEA under ion irradiations up to a dose of 500 dpa for temperatures between 475–580 °C. The void swelling resistance of this HEA is notably better than the austenitic stainless steels and comparable to the oxide dispersion-strengthened steels that are challenging and more expensive to fabricate. Therefore, the $NiCoFeCrCu_{0.12}$ HEA is chosen for investigation under the current work package.

3.2 Experimental

Cast rods of $NiCoFeCrCu_{0.12}$ HEA fabricated by vacuum induction melting were procured from sophisticated alloys for this study. The cast microstructures are typically non-homogeneous, and performing homogenization annealing therefore becomes inevitable in most cases. Due to the large size of the as-cast material (nearly 30 inches in length), the microstructure can vary significantly along the length and width of the sample. Further, implementation of a single solution treatment on such a large as-cast material can result in microstructural variation. The motivation of this work is determining the as-cast and solution-treated specimen from the extreme end and the middle part of the rod, because this will serve as the starting condition of the material for the ShAPE experiments. Results presented in this report focus on the middle part of the as-cast rod that reveals the compositionally non-homogenous microstructure of the

$NiCoFeCrCu_{0.12}$ HEA. The microstructure of the extreme parts of the as-cast rod will be studied in future work.

Due to the lack of experimental data in the literature, Thermo-Calc™ software was utilized to assess the homogenization temperature. The pseudo-binary phase diagram ($NiFeCoCu_{0.12}$ with Cr addition) was generated by Thermo-Calc™ using the TCHEA3 database and is presented in Figure 14. The vertical dotted line (at 24.25% of Cr) represents the $NiCoFeCrCu_{0.12}$ HEA. It was evident that the solvus or the homogenization temperature for $NiCoFeCrCu_{0.12}$ HEA is ~1090 °C, as indicated by the dotted horizontal line on the phase diagram. Because there could be discrepancies in the predicted and experimentally observed temperatures, a temperature of 1200 °C and a duration of 6 h was chosen for homogenizing the as-cast microstructures of this HEA.

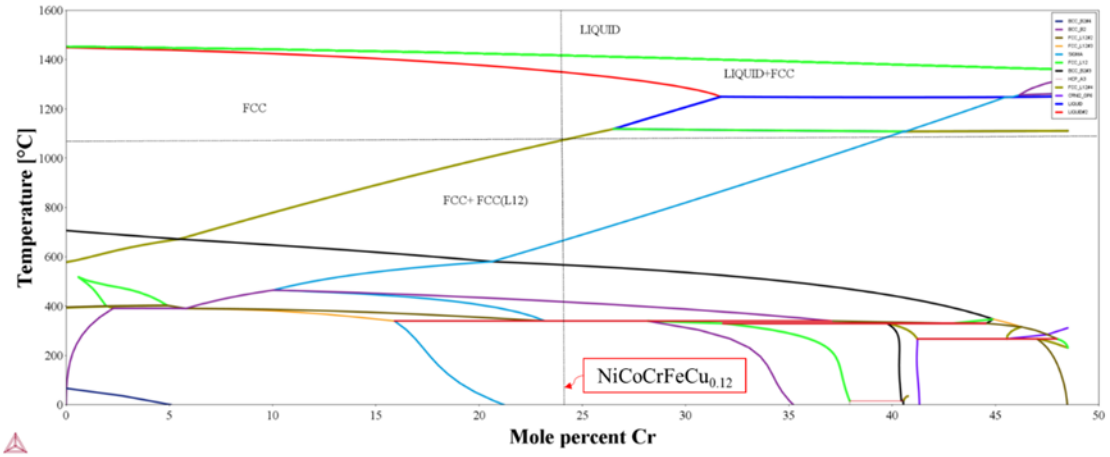

Figure 14. Pseudo-binary phase diagram generated using Thermo-Calc software.

3.2.1 Characterization Technique

Optical imaging and differential interference contrast (DIC) imaging were done using OLYMPUS DSX100. A JEOL 7600 scanning electron microscope (SEM) was used to collect images and orientation mappings of the polished samples. Both backscatter electron and secondary electron imaging were used for microstructural characterization. Electron backscatter diffraction analysis was performed using AZtecCrystal software from Oxford Instruments. The hardness testing was performed using a CLARK CM-802AT automatic hardness tester, and 500 gf of load was used.

3.2.2 Results

Figure 15(a) shows the schematic of the as-cast rod and the section from the middle section of the rod that was cut for the heat treatment study. Figure 15(b) shows the optical image of the as-cast sample that reveals a negligible number of defects, and Figure 15(c) shows the DIC overlay that reveals the dendritic structure in the as-cast sample. Figure 15(d) is a montage of SEM images capturing the entire sample. This image reveals the nature of grain structures in this section of the as-cast rod. The grain appears to be elongated and irregularly shaped toward the inner side of the sample, while the grain sizes decrease toward the outer region of the sample. This is possibly due to the thermal gradient generated through solidification during the

casting process. The magnified SEM image in Figure 15(e) shows the presence of grain striations in the as-cast sample.

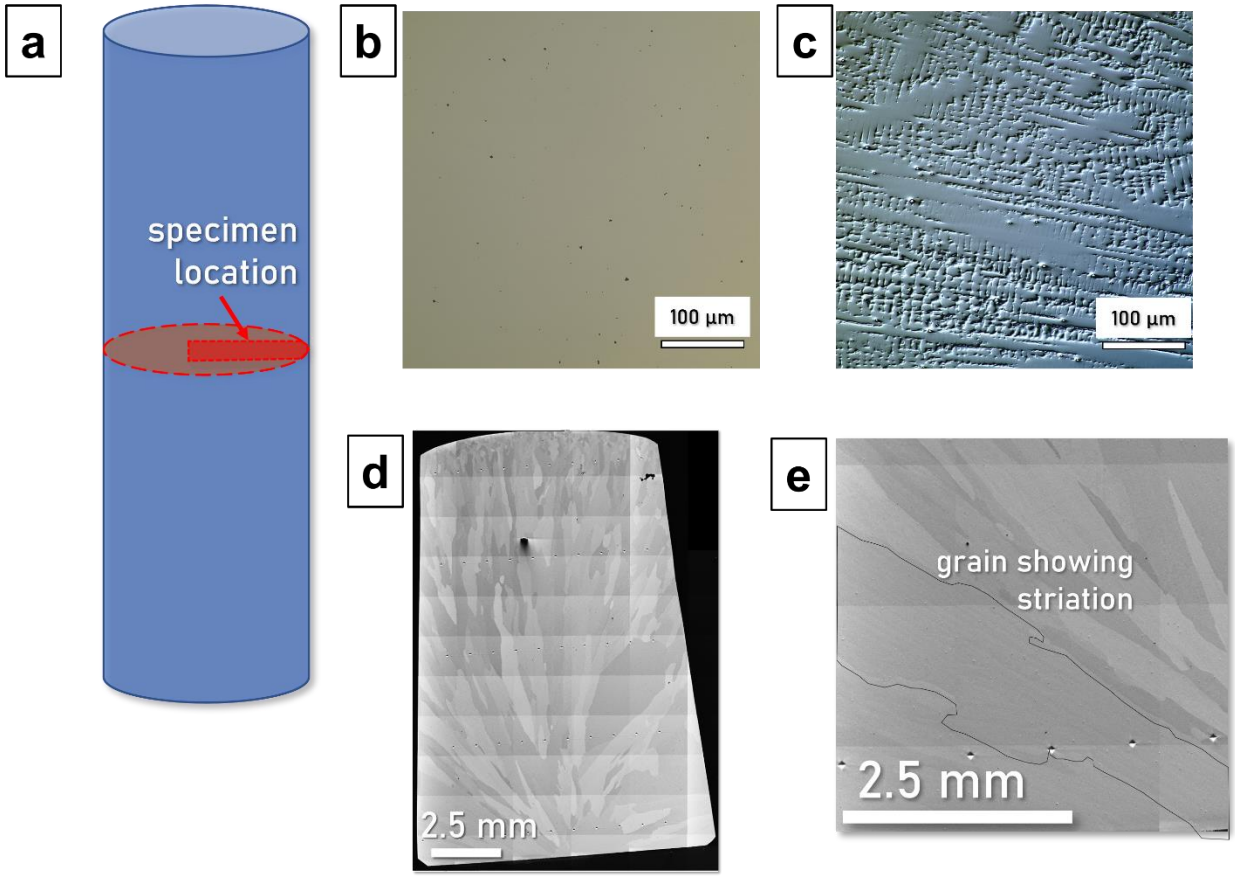

Figure 15. (a) A schematic of the cut section of the as-cast rod for heat treatments, (b) an optical image of the sample shows a very negligible amount of pores in the sample, (c) the DIC layover shows the dendritic structures in the as-cast alloy, (d) the montage SEM image of the as-cast alloy shows the grain structure of the sample, and (e) a magnified SEM image shows the elongated grains in the sample with grain striations.

Figure 16 shows the inverse pole figure of the as-cast sample that reveals the grain sizes and shape more accurately. The grain size variation from the inner to outer region of the as-cast sample is clearly revealed. So, it can be concluded that there is significant texturing along the radial direction of the as-cast material.

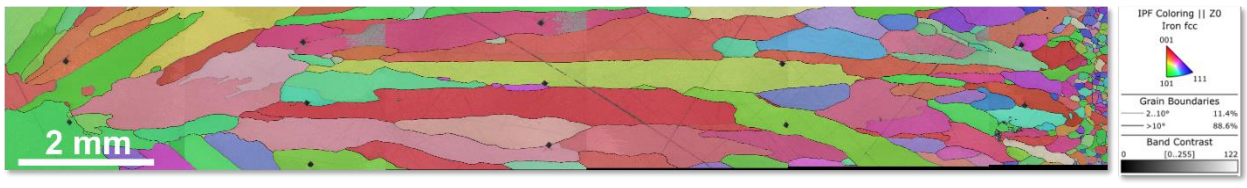

Figure 16. The orientation map of the as-cast sample reveals the variation of grain size from the inner to outer region of the rod.

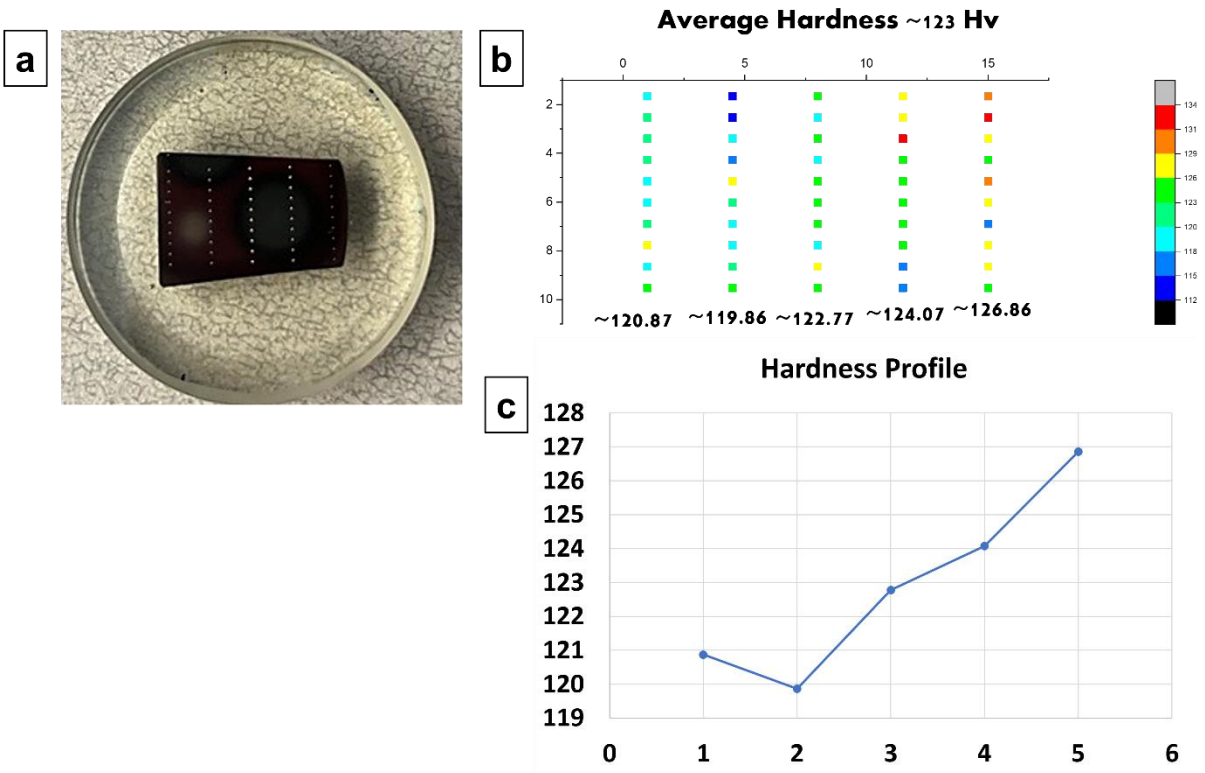

Figure 17. (a) Image of the as-cast sample with the location of indents from the hardness measurement, (b) the map of the indent with hardness values, and (c) a plot of hardness values of the as-cast alloy from the inner to outer region.

Figure 17(a) shows the photograph of the as-cast sample with indents for hardness measurement along the entire sample. Figure 17(b) shows the map that reveals the location of each indent and the values of hardness corresponding to each indent. Figure 17(c) is a plot that shows the variation of hardness value from the inner column to the outer columns of the indents. The hardness appears to increase gradually from the inner to outer region, and that is possibly due to a corresponding decrease in grain sizes. The higher densities of grain boundaries toward the outer side can contribute to higher hardness values.

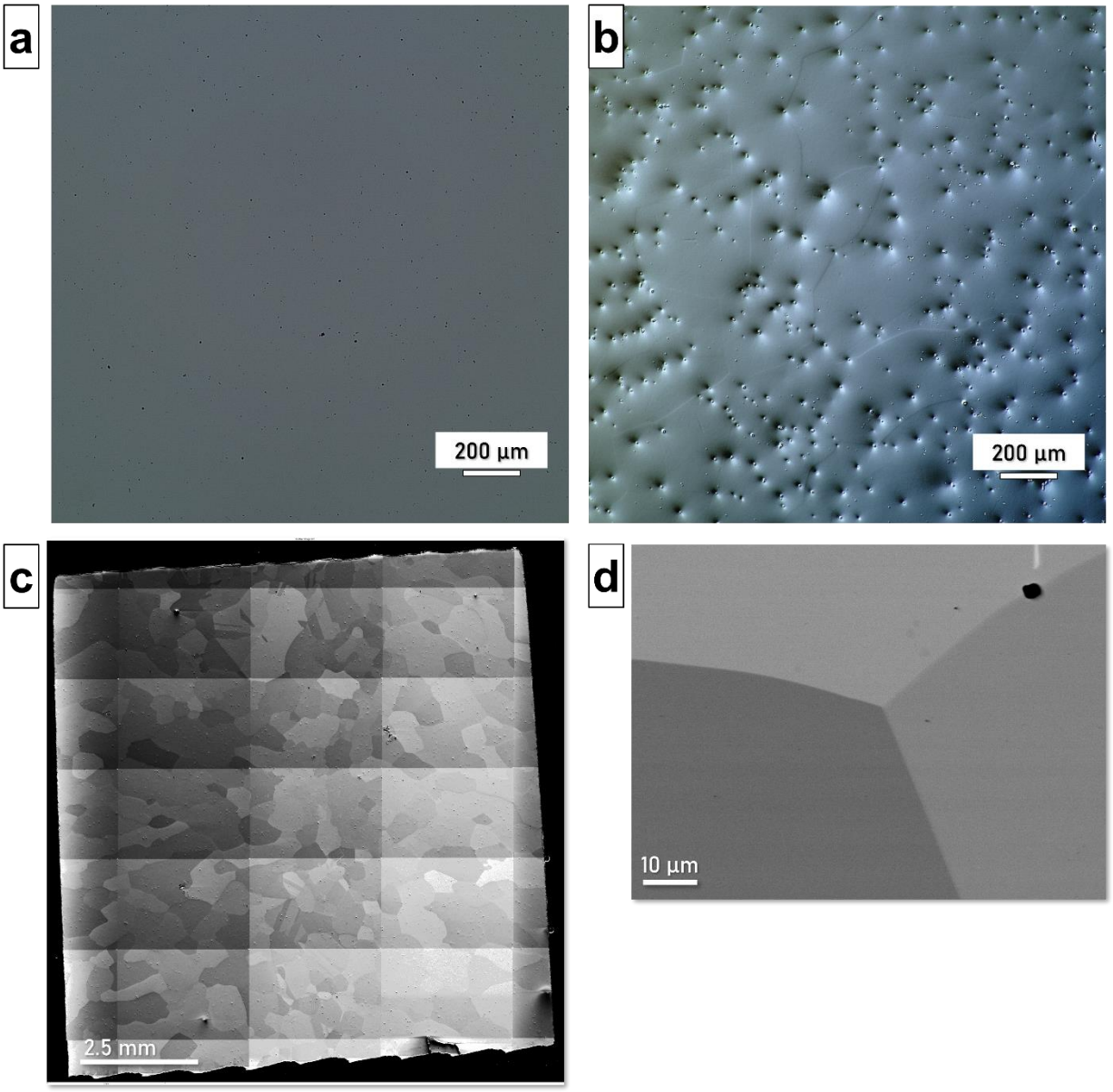

Figure 18. (a) an optical image of the heat-treated sample shows a very negligible amount of pores in the sample, (b) the DIC layover does not show any dendritic structure that was found in the as-cast alloy, (c) the montage SEM image of the heat-treated sample shows the equiaxed grain structure of the sample, and (d) a magnified SEM image shows no grain striation in the sample.

Figure 18(a) shows the optical image of the heat-treated sample, and Figure 18(b) shows the DIC overlay that does not show any dendritic microstructure, as opposed to that found in the as-cast sample in Figure 16(c). Figure 18(c) is a montage of SEM images of the heat-treated sample that clearly shows that the elongated grains observed in as-cast samples are no longer present in the heat-treated sample and that most of the grains appear to be equiaxed in nature. Figure 18(d) is a magnified SEM image without grain boundary striations, as opposed to the as-cast sample. Therefore, the heat treatment in this study appears to remove the dendritic structure and recrystallize the grains.

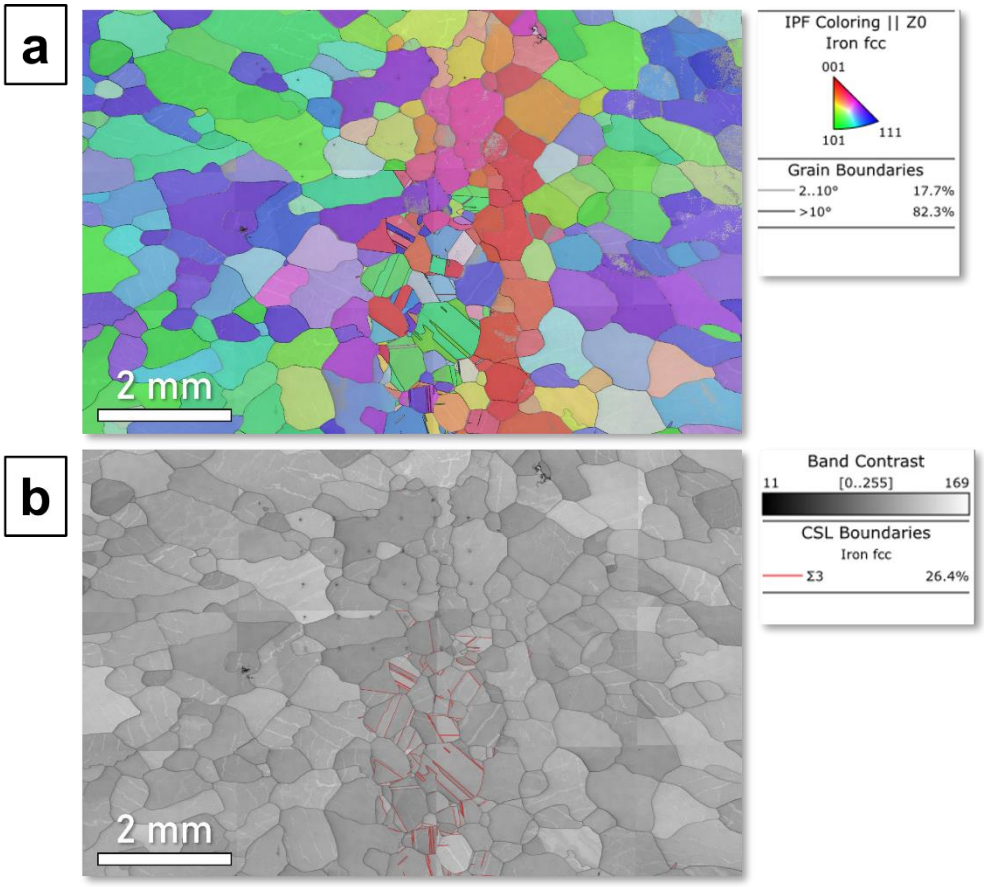

Figure 19. (a) The inverse pole figure and (b) the band contrast image of the heat-treated sample reveals the near equiaxed grains from the inner to outer region of the rod. The middle region of the sample reveals a higher concentration of ∑3 type grain boundaries.

Figure 19(a) is the inverse pole figure of the heat-treated sample that shows the refined grains. Interestingly, Figure 19(b) shows the presence of a higher number of twin boundaries near the center of the sample where the number of ∑3 type grain boundaries is high. Further examination is required to understand the formation mechanism of such twin boundaries in this heat-treated sample.

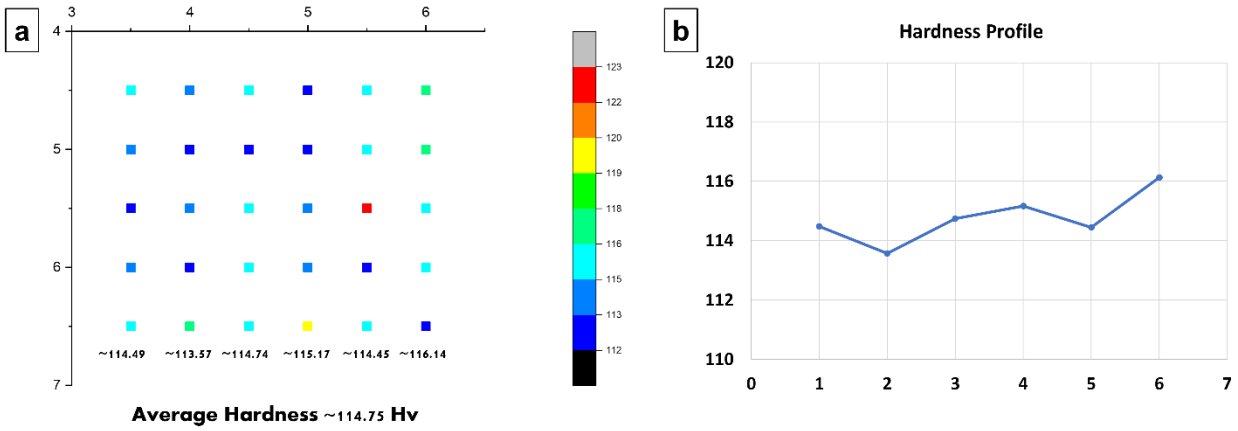

Figure 20. (a) A map of the indent with hardness values in the heat-treated sample, and (b) a plot of the hardness values of the heat-treated sample from the inner to outer region.

Figure 20(a) shows the map that reveals the location of each indent and the values of hardness corresponding to each indent. Figure 20(b) is a plot that shows the variation of hardness value from the inner column to the outer columns of the indents. It can be seen here that the hardness value does not seem to vary significantly from the inner to the outer region. This is possibly due to the homogeneous grain size after the recrystallization heat treatment.

3.2.3 Functionally Graded Materials (FGMs)

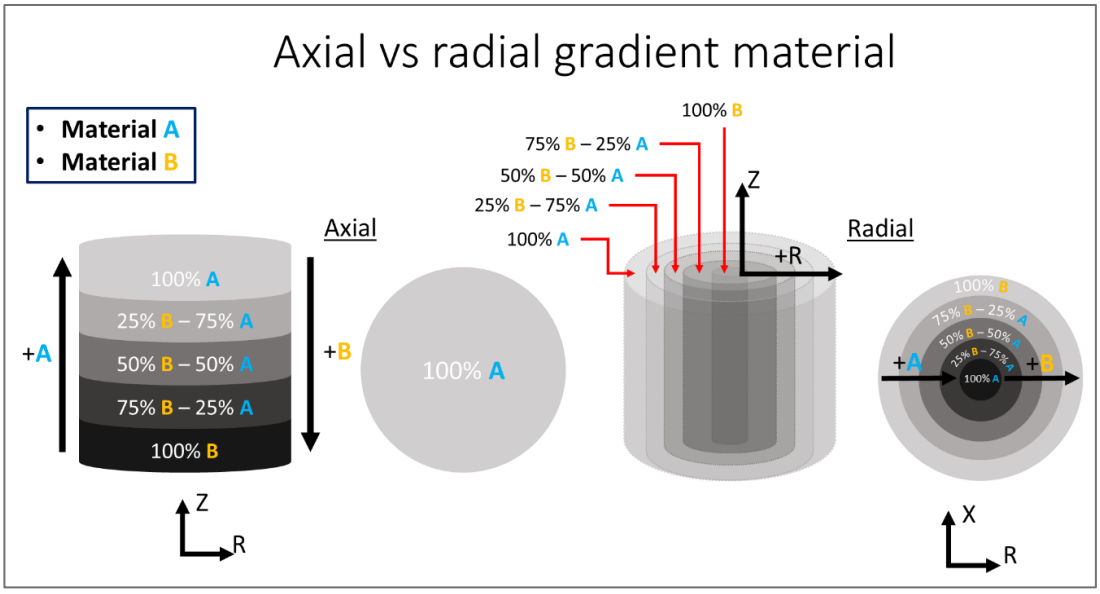

Figure 21. Differences between axial and radial gradient material.

FGMs with variable properties along specific directions within their volume have applications in various industries, including nuclear, marine, electrical, and biomedical sectors [34]. The application space is also anticipated to expand to other industries. Certain structural materials in marine (marine riser pipelines [35]) and nuclear applications require strength at the core and

corrosion/radiation resistance on the surface layers. Numerical simulations also indicate that FGMs decrease the thermal stresses and increase the component's lifetime when a suitable choice for the composition of the graded layer is made [36-38]. A gradual shift in the compositions and properties either axially or radially (as shown in Figure 21) is ideal for maintaining the component's structural integrity during the service. However, the current technology involving thermal spray coatings [39], laser cladding [40], laser AM [41], chemical [42] and physical vapor deposition [43], sheet lamination [44], centrifugal casting [45], etc., is not cost-effective and requires significant process parameter optimization, as well as pre-and post-processing of the component.

Moreover, **no existing techniques have been explored to fabricate radially gradient materials except centrifugal casting [34]**. While centrifugal casting has been employed to fabricate radially gradient materials, the materials systems are limited to metal–ceramic combinations only because the gradient formation is based on the densities and movement of the ceramic particles in the liquid metal. In other words, the centrifugal casting fails to fabricate metal–metal or metal–alloy functionally gradient materials. **Considering this, we have designed a new approach that will be the first invention to manufacture radially gradient systems via powder metallurgy routes and is simple, cost-effective, versatile, and straightforward [46]**

Bulk FGMs with discontinuous gradients [47] can be easily manufactured via powder metallurgy (PM) techniques. However, as previously stated only axially gradient structures have been produced via PM techniques. Powders are weighed and mixed using a pre-designed spatial distribution of the desired geometry. The mixed powders are then packed differently depending upon the PM technique employed and sintered to obtain a consolidated structure [48]. The advantages of PM FGMs are that they can have multiple distinct layers, produce layers of different thicknesses, and have low residual stresses during the sintering process. Hot isostatic pressing (HIP) [49] and spark plasma sintering (SPS) [50,51] are the most advanced and popular PM techniques available today.

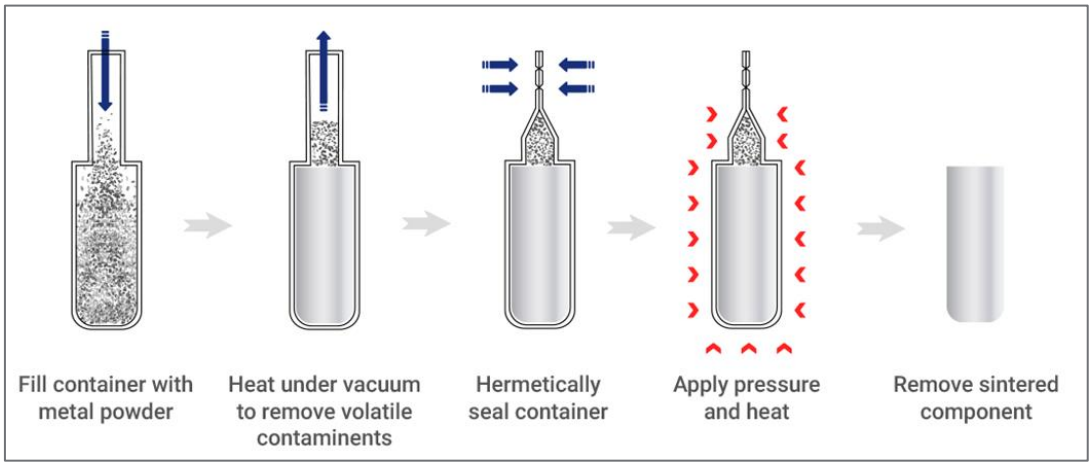

Figure 22. Processing steps involved in hot isostatic pressing.

The HIP process involves two significant steps. The first one is filling the HIP can/container (made of carbon steel typically) with the desired metal/alloy powders and then sintering at high temperatures under isostatic pressure, as illustrated in Figure 22 [52]. The powder container is filled with the desired metal/alloy powder, and the container is placed under vacuum to remove

contaminants. The container is finally sealed by welding the top and placed inside the HIP furnace for HIPing. After the HIPing, the container is removed from the furnace after cooling. An optimized HIP process results in a fully densified part. SPS is also similar to HIP, and a combination of heat and pressure is utilized to consolidate the powders. However, there are a few distinct differences. Instead of externally applied heat, a pulsed direct current (DC) passes through a graphite die and compacted powder, which internally heats the powder to sinter [54]. Additionally, in the SPS, the powders are loaded into the graphitic dyes as opposed to the carbon steel container in the HIP process. Nevertheless, the powder loading mechanism remains the same between the two processes—powders are vertically loaded into the dies/containers before the sintering process. We therefore have designed a novel approach to load powders vertically that could be utilized to fabricate radially gradient materials via PM techniques such as HIP and SPS.

3.2.3.1 Radial Gradient Design

Powder loading mechanism: The proposed mechanism for loading metal alloy powders is carried out in discrete steps; each step forms a distinct composition and in combination provides the whole radial gradient structure. The powder loading mechanism consists of multiple

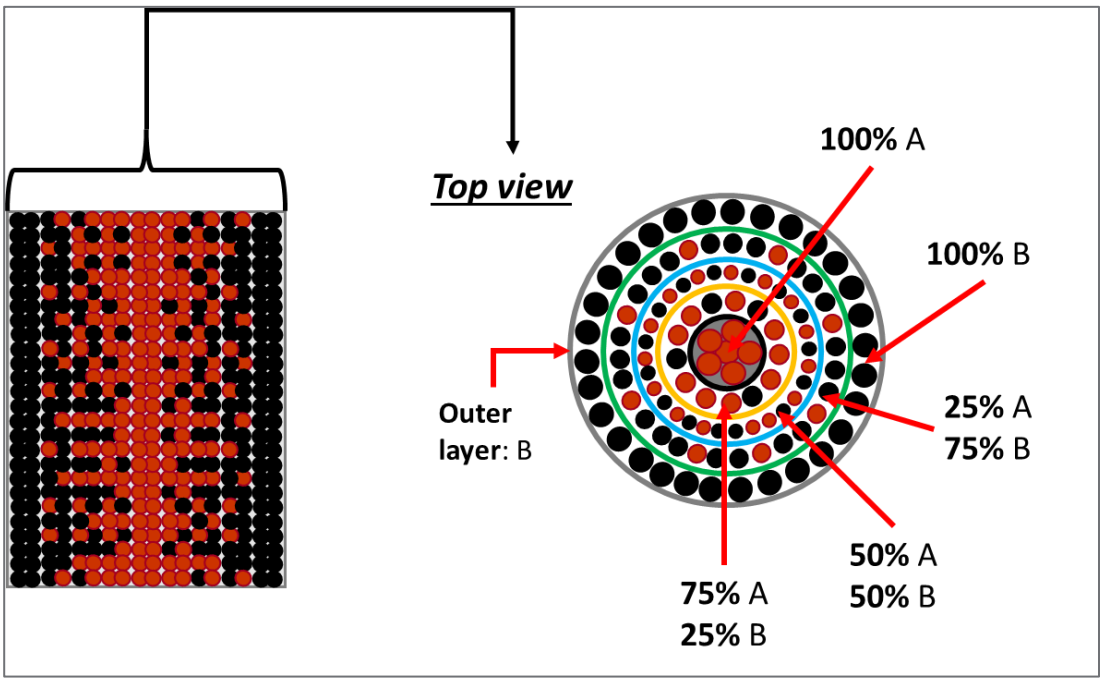

Figure 23. A schematic illustration showing different views of a container loaded with powders in a radial manner.

concentric circular dividers with defined height and wall thickness. The purpose of the dividers is to isolate individual metal alloy powders. The circular dividers are designed taller than the height of the powder loading medium (e.g., powder container in HIP or graphite die in SPS). The dividers are additionally sectioned with different heights for easy removal and are placed in a descending order by height, i.e., the tallest divider is placed at the center and the shortest is

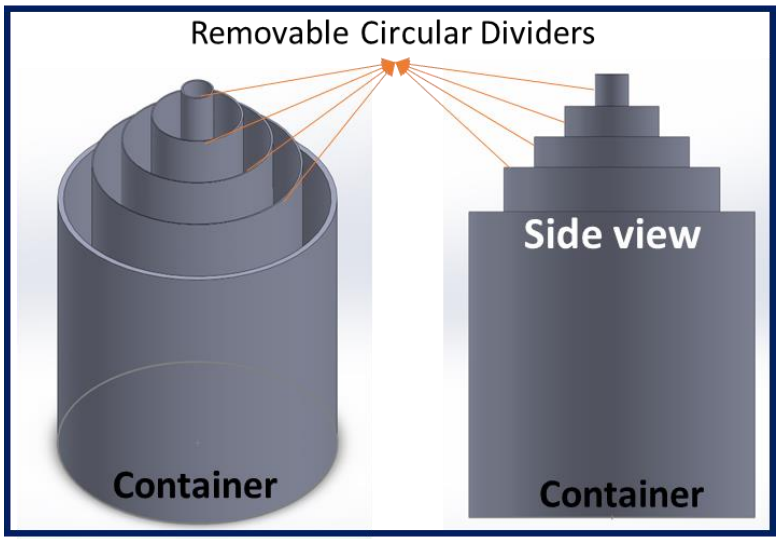

Figure 24. Schematic of the concentrically placed sheet dividers inside a container

placed near to the periphery of the container, as shown in Figure 23. The number of dividers placed determines the number of discrete compositional steps in the radial gradient structure. Once the dividers are firmly placed with the intended spacings, the metal alloy powders of different compositions are loaded and filled into individual circular hollow regions in between the dividers. The powders must be filled in a sequential order to avoid any movement of the circular dividers until all regions are filled; innermost (center) region is filled first, and the outermost (periphery) region is filled last in that order. The cylindrical partitions are also removed consecutively, starting from the innermost divider to the outermost divider. This will allow the powders to settle with minimal spread into the adjacent regions. The successful removal of all the circular dividers marks the completion of the powder loading mechanism. The container now has the powders arranged in a radially gradient manner (as illustrated in Figure 24) which upon HIP would produce a consolidated radial FGM. Note that only two different materials A and B and gradients with a 25% change in composition per step are shown in Figure 24, which is only for illustration purposes, and that this approach is practically not limited to those conditions.

3.2.3.2 Proof-of-Concept Study

We performed a benchtop experiment to prove the proposed powder loading mechanism. Because it is only a proof-of-concept study to validate the powder loading mechanism, HIP processing was not considered as a part of this experiment.

Silica sand particles were utilized instead of the metal alloy powders to (1) limit the wasting of hazardous materials and (2) make it cost-effective. The silica sand particles (Hygloss) chosen were between 100–500 µm, which is somewhat like the size range of the metal alloy powders that are typically used for HIP and other PM processing. Furthermore, two different colors—yellow and brown—were chosen for the sands to mimic the different compositions of the radial gradient. A 500 mL lab glass beaker (Karter Scientific; Lake Charles, LA) was used as an alternative to the carbon steel container to host the powders. Cardboard tubes with 2” and 3” diameters procured from Uline were used as the circular dividers for this experiment. A schematic of the proposed benchtop experiment is shown in

Figure 25. The idea is to follow the proposed powder loading mechanism closely and achieve a radial gradient with brown sand particles at the center and yellow sand particles at the periphery of the glass beaker. A side view of the beaker with circular dividers is shown in Figure 26. The beaker's interior was separated into two concentric circular regions using the 2" and 3" cardboard tubes.

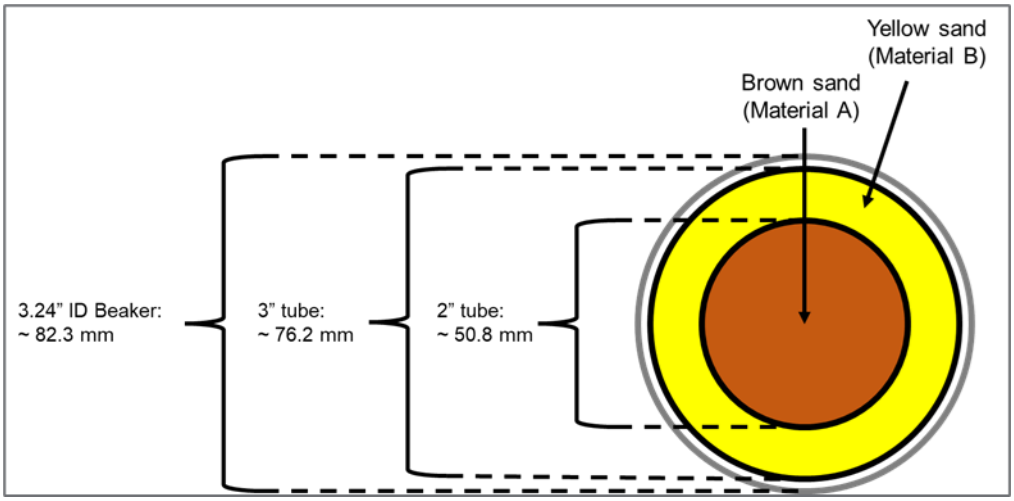

Figure 25. Schematic of the benchtop experiment.

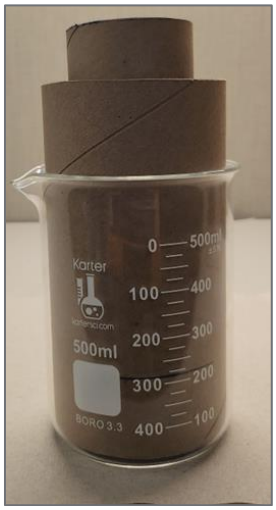

Figure 26. A side view of the beaker (container) with two circular dividers.

The silica powders were loaded using a ~0.5" diameter stainless steel funnel spout in each region. When both the regions were filled with sand particles, the circular dividers are slowly removed; the innermost 2" divider was removed first followed by the outermost 3" divider. The different views of the beaker after successful loading of the sand particles and the removal of dividers are shown in Figure 27. The top and bottom views reveal a perfect radial gradient with brown sands at the center and yellow sands on the outer side, proving the proposed concept. The side view presented in Figure 27 shows a slightly inclined and mountain-like top surface for the brown sands at the center that could be easily optimized for flat loading. The results of this benchtop experiment clearly determine the feasibility of the proposed loading mechanism for radially loading metal alloy powders for producing radial FGMs via PM techniques.

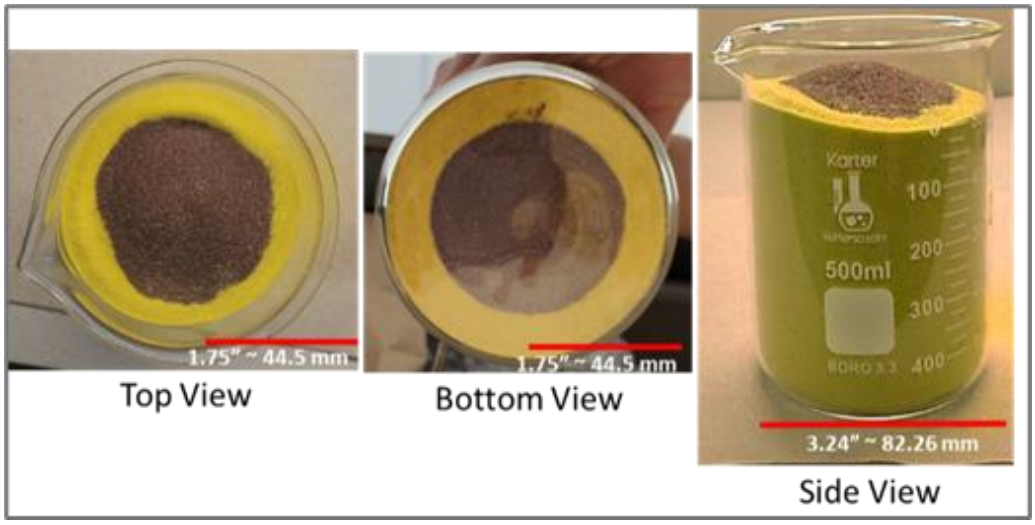

Figure 27. Different views of the beaker with radially loaded sand particles.

4.0 Perform ShAPE and FSAM Experiments

4.1 FSAM

The approach devised for the FSAM experiments also suffers from the lack of previous experience in terms of processing parameters for the unique composition of the HEA alloy select for this investigation. Furthermore, the ambitious schedule envisaged for this project requires an accelerated experimental approach, i.e., a simplified process parameters optimization procedure. Therefore, initial process parameters will be based on values reported in the literature for friction welding of a comparable HEA composition. Friction welding is a solid phase joining process and the initial plasticization stage is comparable to those observed in FSAM. Based on these start parameters rotational speed will be progressively increased, by constant axial force, until the onset of plasticization is reached. This will define the so-called “ramp” parameters, i.e., parameters to be employed before the translation motion is started. Once plasticization has been achieved, the translatory movement will be activated at low deposition speeds and constant axial force and rotational speed. Once an optimized process parameter set has been established successive layers will be deposited on top of each other to produce samples for the characterization activities.

4.2 ShAPE

The $NiCoFeCrCu_{0.12}$ HEA rods for ShAPE and friction surfacing layer deposition were obtained from sophisticated alloys. Initial homogenization experiments confirmed that 1200 °C for 6 hours led to the removal of dendritic segregation. Therefore, the rods for ShAPE and friction surfacing layer deposition feedstock were subjected to this heat treatment to eliminate any chemical inhomogeneity. Then billets of height 23 mm, outer diameter 31.6 mm, and inner diameter 10.26 mm were machined using CNC machines. ShAPE tooling consists of an extrusion die, mandrel, liner, and backer. Because the Cu HEA is a high-temperature material, we have selected tooling materials that could sustain high processing temperatures and forces. W-La2O3 was used to make both the extrusion die and mandrel, and IN718 was used to make the liner and backer. This is the first time ShAPE will be performed on a high-entropy alloy—thus, obtaining a correct set of processing conditions for the first trial is not possible. Lessons learned from extruding a PM2000 ODS alloy will be utilized. The Cu HEA is expected to be weaker than ODS steel, and the rotational speed will therefore be changed from 400 rpm (in the case of ODS) to 200 rpm (for Cu HEA), while the ram speed will be maintained at around 5 mm/min. Lessons learned from the first experiment will guide the process parameter selection for the next set of experiments.

5.0 Performance Evaluation and Validation

5.1 Corrosion

Two different corrosion tests will be performed as part of this work. Potentiodynamic polarization testing will be performed on a spectrum of samples. Testing will be performed in sulfuric acid at room temperature. A comparison of the generated curves will provide a baseline for how the different changes affect corrosion potential. The second tests will be aqueous immersion testing. Samples will be placed in a non-stirred pressure vessel filled with PWR water. The vessels will be heated to 275 °C for 150+ hours. These samples will then be removed and examined with XRD as well as being sectioned and polished for SEM imaging, generating data about the composition and structure of the oxide layers that form.

Initial raw material has been purchased, and corrosion testing as a benchmark will be evaluated between the as-cast structure and homogenization microstructures, according to the sampling plan in Figure 28. These tests will be performed in the following months.

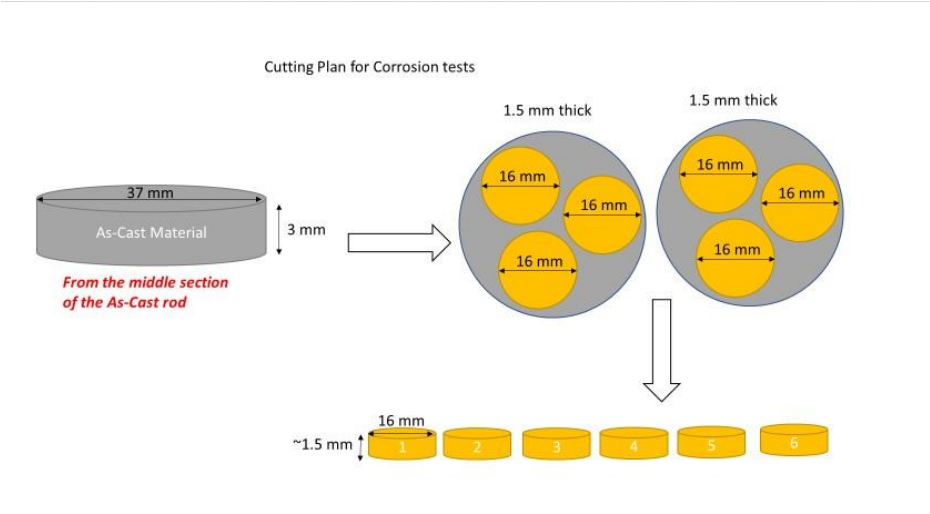

Figure 28. Cutting plan for corrosion tests on the raw material.

6.0 Outlook

The future planned work includes:

- Microstructural evaluation of the extreme end of the as-cast and subsequently heat-treated rod.
- Thermal diffusivity measurements are essential for modeling ShAPE processing of the $NiCoFeCrCu_{0.12}$ HEA. The modeling work will help optimize the process parameters for the ShAPE process. Because the $NiCoFeCrCu_{0.12}$ HEA considered for this project is novel and hardly any thermal diffusivity data is available in the literature, conducting these preliminary experiments becomes crucial. In addition, the Differential scanning calorimetry experiments will provide heat capacity information, which offers insights into the thermal stability of the Cu-rich nano precipitates in this HEA. This information will be helpful in designing the annealing heat treatments for further enhancing the properties. Idaho National Laboratory has been identified as having the capabilities to perform both experiments with the following objectives:
    - Thermal diffusivity measurements need to be performed at 100 °C intervals from 25 °C to 500 °C and 50 °C intervals from 500 °C to 1000 °C.
    - Differential scanning calorimetry heat capacity measurements need to be performed continually from 25 °C to 1000 °C.
- Future radial powder HIP activities
    - Finalize university/industry partners to host the HIP experiments utilizing metal alloy powders.
    - Procure the customized dividers to assemble the powder loading mechanism.
    - Send powder can and HIP parameters to HIP manufacturer and load the metal powders using the proposed mechanism.
    - Characterize the materials properties in-house (hardness, tensile, XRD, SEM).
    - Once the HIP experiments are completed, SPS, hot pressing, and other powder metallurgy approaches may be tried using metal alloy powders.
- Perform first off ShAPE and FSAM experiments and the associated characterization.

The following presentation and journal paper resulted from this work:

- Li L., M. Nartu, M. Komarasamy, A. Soulami, and I. van Rooyen. "Modeling and analysis of the extreme process conditions during the fabrication of high-entropy alloys by Shear Assisted Processing and Extrusion (ShAPE)." TMS 2024, Orlando, Florida, 03/04/2024.
- 2. Li L., M. Nartu, M. Komarasamy, A. Soulami, and I. van Rooyen. "Modeling and analysis of the extreme process conditions during the fabrication of high-entropy alloys by Shear Assisted Processing and Extrusion (ShAPE)." Journal TBD.

7.0 References

[1] Kombaiah, B., Zhou, Y., Jin, K., Manzoor, A., Poplawsky, J. D., Aguiar, J. A., Bei, H., Aidhy, D. S., Edmondson, P. D., Zhang, Y., Nanoprecipitates to Enhance Radiation Tolerance in High-Entropy Alloys. ACS Appl Mater Interfaces 2023, 15 (3), 3912-3924.

[2] S. Whalen, et.al., Manufacturing Letters, Accepted In-Press, 2023

[3] S. Whalen, et. al., Journal of Manufacturing Processes, 71, pg. 699-710, 2021.

[4] Komarasamy M., et. al., Light Metals 2022, 308-313

[5] Qiu, Y., Thomas, S., Gibson, M. A., Fraser, H. L., Birbilis, N., Corrosion of high entropy alloys. npj Materials Degradation 2017, 1 (15).

[6] Hsu, Y.-J., Chiang, W.-C., Wu, J.-K., Corrosion behavior of FeCoNiCrCux high-entropy alloys in 3.5% sodium chloride solution. Materials Chemistry and Physics 2005, 92 (1), 112-117.

[7] Li, L., et al., "Analysis of contact conditions and microstructure evolution in shear assisted processing and extrusion using smoothed particle hydrodynamics method" Materials & Design, Volume 221, 2022

[8] Li, L., et al., "Meshfree simulation and experimental validation of extreme thermomechanical conditions in friction stir extrusion" Computational Particle Mechanics, 1-21, 2021.

[9] Ralston, K. D., Birbilis, N., Effect of Grain Size on Corrosion: A Review. Corrosion 2010, 66 (7).

[10] Bohni, H., Localized Corrosion of Passive Metals. In Uhligh's Corrosion Handbook, 3rd ed.; Revie, R. W., Ed. John Wiley & Sons: Hoboken, New Jersey, 2011; pp 157-169

[11] Xie, J., Zhang, S., Dong, J., Wang, S., Wang, H., Kuang, W., Insights into the superior stress corrosion cracking resistance of FeCrAl alloy in high temperature hydrogenated water: The critical role of grain boundary oxidation. Corrosion Science 2022, 208.

[12] Lehockey, E. M., Palumbo, G., Lin, P., Brennenstuhl, A. M., On the relationship between grain boundary character distribution and intergranular corrosion. Scripta Materialia 1997, 36 (10), 1211-1218

[13] Kalsar, R., Ma, X., Darsell, J., Zhang, D., Kappagantula, K., Herling, D. R., Joshi, V. V., Microstructure evolution, enhanced aging kinetics, and mechanical properties of AA7075 alloy after friction extrusion. Materials Science & Engineering A 2022, 833, 142575

[14] Liu, M.B., Liu, G.R., Smoothed particle hydrodynamics (SPH): An overview and recent developments. Arch Comput Methods Eng 2010;17:25–76.

[15] Yu, P., Zhuang, Y., Chou, J.P., Wei, J., Lo, Y.C. and Hu, A., 2019. The influence of dilute aluminum and molybdenum on stacking fault and twin formation in FeNiCoCr-based high entropy alloys based on density functional theory. Scientific reports, 9(1), p.10940.

[16] MatWeb: Material property data. https://www.matweb.com/.

[17] Kim, Y.-K., M.-C. Kim, and K.-A. Lee, 1.45 GPa ultrastrong cryogenic strength with superior impact toughness in the in-situ nano oxide reinforced CrMnFeCoNi high-entropy alloy matrix nanocomposite manufactured by laser powder bed fusion. Journal of Materials Science & Technology, 2022. 97: p. 10-19.

[18] Ye, Y.F., et al., High-entropy alloy: challenges and prospects. Materials Today, 2016. 19(6): p. 349-362.

[19] Yao, M.J., et al., A novel, single phase, non-equiatomic FeMnNiCoCr high-entropy alloy with exceptional phase stability and tensile ductility. Scripta Materialia, 2014. 72-73: p. 5-8.

[20] Deng, Y., et al., Design of a twinning-induced plasticity high entropy alloy. Acta Materialia, 2015. 94: p. 124-133.

[21] Shi, Y., B. Yang, and P.K. Liaw Corrosion-Resistant High-Entropy Alloys: A Review. Metals, 2017. 7, DOI: 10.3390/met7020043.

[22] Ostovari Moghaddam, A., et al., High temperature oxidation resistance of W-containing high entropy alloys. Journal of Alloys and Compounds, 2022. 897: p. 162733.

[23] Pickering, E.J., et al. High-Entropy Alloys for Advanced Nuclear Applications. Entropy, 2021. 23, DOI: 10.3390/e23010098.

[24] Kumar, N.A.P.K., et al., Microstructural stability and mechanical behavior of FeNiMnCr high entropy alloy under ion irradiation. Acta Materialia, 2016. 113: p. 230-244.

[25] Zhang, Y., et al., Atomic-level heterogeneity and defect dynamics in concentrated solid-solution alloys. Current Opinion in Solid State and Materials Science, 2017. 21(5): p. 221-237.

[26] Fan, Z., et al., From suppressed void growth to significant void swelling in NiCoFeCr complex concentrated solid-solution alloy. Materialia, 2020. 9: p. 100603.

[27] Parkin, C., et al., Phase stability, mechanical properties, and ion irradiation effects in face-centered cubic CrFeMnNi compositionally complex solid-solution alloys at high temperatures. Journal of Nuclear Materials, 2022. 565: p. 153733.

[28] Kombaiah, B., et al., Phase stability of single phase Al0.12CrNiFeCo high entropy alloy upon irradiation. Materials & Design, 2018. 160: p. 1208-1216.

[29] El-Atwani, O., et al., Outstanding radiation resistance of tungsten-based high-entropy alloys. Science Advances. 5(3): p. eaav2002.

[30] Chen, D., et al., Effects of minor alloying addition on He bubble formation in the irradiated FeCoNiCr-based high-entropy alloys. Journal of Nuclear Materials, 2020. 542: p. 152458.

[31] Gwalani, B., et al., Optimizing the coupled effects of Hall-Petch and precipitation strengthening in a Al0.3CoCrFeNi high entropy alloy. Materials & Design, 2017. 121: p. 254-260.

[32] Gwalani, B., et al., High density of strong yet deformable intermetallic nanorods leads to an excellent room temperature strength-ductility combination in a high entropy alloy. Acta Materialia, 2021. 219: p. 117234.

[33] Choudhuri, D., et al., Formation of a Huesler-like L21 phase in a CoCrCuFeNiAlTi high-entropy alloy. Scripta Materialia, 2015. 100: p. 36-39.

[34] Naebe, M. and K. Shirvanimoghaddam, Functionally graded materials: A review of fabrication and properties. Applied Materials Today, 2016. 5: p. 223-245.

[35] Chandrasekaran, S., S. Hari, and M. Amirthalingam, Wire arc additive manufacturing of functionally graded material for marine risers. Materials Science and Engineering: A, 2020. 792: p. 139530.

[36] Itoh, Y., M. Takahashi, and H. Takano, Design of tungsten/copper graded composite for high heat flux components. Fusion Engineering and Design, 1996. 31(4): p. 279-289.

[37] Ueda, S., Elastoplastic Analysis of W-Cu Functionally Graded Materials Subjected to a Thermal Shock by Micromechanical Model. Journal of Thermal Stresses, 2001. 24(7): p. 631-649.

[38] Chapa, J. and I. Reimanis, Modeling of thermal stresses in a graded Cu/W joint. Journal of Nuclear Materials, 2002. 303(2): p. 131-136.

[39] Matějíček, J., P. Chráska, and J. Linke, Thermal Spray Coatings for Fusion Applications—Review. Journal of Thermal Spray Technology, 2007. 16(1): p. 64-83.

[40] Pei, Y.T. and J.T.M. De Hosson, Functionally graded materials produced by laser cladding. Acta Materialia, 2000. 48(10): p. 2617-2624.

[41] Nartu, M.S.K.K.Y., et al., Directed-Energy Deposition, in Additive Manufacturing in Biomedical Applications. 2022, ASM International. p. 0.

[42] Sasaki, M. and T. Hirai, Thermal fatigue resistance of CVD SiC/C functionally gradient material. Journal of the European Ceramic Society, 1994. 14(3): p. 257-260.

[43] Dobrzański, L.A., et al., Structure and mechanical properties of gradient PVD coatings. Journal of Materials Processing Technology, 2008. 201(1): p. 310-314.

[44] Zhang, Y. and J. Wang, Fabrication of Functionally Graded Porous Polymer Structures using Thermal Bonding Lamination Techniques. Procedia Manufacturing, 2017. 10: p. 866-875.

[45] Watanabe, Y., N. Yamanaka, and Y. Fukui, Control of composition gradient in a metal-ceramic functionally graded material manufactured by the centrifugal method. Composites Part A: Applied Science and Manufacturing, 1998. 29(5): p. 595-601.

[46] Nartu, M., Van Rooyen, I., Yoon, D., A Novel Metal Powder Loading Mechanism for Fabrication of Radially Gradient Systems, Provisional Patent Application number: 63/539,052.

[47] Mahamood, R.M., et al. Functionally Graded Material: An overview. 2012.

[48] Dewidar, M.M., H.-C. Yoon, and J.K. Lim, Mechanical properties of metals for biomedical applications using powder metallurgy process: A review. Metals and Materials International, 2006. 12(3): p. 193-206.

[49] Samal, P. and J. Newkirk, Powder metallurgy processing by hot isostatic pressing. 2015.

[50] Guillon, O., et al., Field-Assisted Sintering Technology/Spark Plasma Sintering: Mechanisms, Materials, and Technology Developments. Advanced Engineering Materials, 2014. 16(7): p. 830-849.

[51] Suárez, M., et al., Challenges and Opportunities for Spark Plasma Sintering: A Key Technology for a New Generation of Materials, in Sintering Applications, E. Burcu, Editor. 2013, IntechOpen: Rijeka. p. Ch. 13.

[52] Hot Isostactic Pressing, https://www.levigatealloys.com/hot-isostatic-pressing

Pacific Northwest National Laboratory

902 Battelle Boulevard
P.O. Box 999
Richland, WA 99354

1-888-375-PNNL (7665)

www.pnnl.gov